Huan, Siqi; Mattos, Bruno D.; Ajdary, Rubina; Xiang, Wenchao; Bai, Long; Rojas, Orlando J.

Two-Phase Emulgels for Direct Ink Writing of Skin-Bearing Architectures

Published in:
Advanced Functional Materials

DOI:
10.1002/adfm.201902990

Published: 04/10/2019

Document Version
Peer-reviewed accepted author manuscript, also known as Final accepted manuscript or Post-print

DOI: 10.1002/ ((please add manuscript number))
Article type: Full Paper

Two-Phase Emulgels for Direct Ink Writing of Skin-bearing Architectures

Siqi Huan, Bruno D. Mattos, Rubina Ajdary, Wenchao Xiang, Long Bai, Orlando J. Rojas**

Dr. S. Q. Huan, Dr. B. D. Mattos, R. Ajdary, W. C. Xiang, Dr. L. Bai, Prof. O. J. Rojas
Biobased Colloids and Materials
Department of Bioproducts and Biosystems, Aalto University
Vuorimiehentie 1, Espoo 02150, Finland
Email: rojas.orlando@aalto.fi, long.bai@aalto.fi

Keywords: 3D printing, DIW, two-phase emulgels, Pickering emulsions, controlled delivery

Direct ink writing (DIW) provides programmable and customizable platforms to engineer hierarchically layered constructs. However, one-step, facile synthesis of such architectures *via* DIW has been challenging. Here, we introduce inks based on two-phase emulgels for direct printing and *in-situ* formation of protecting layers enveloping multicomponent cores, mimicking skin-bearing biological systems. The emulgel consists of a Pickering emulsion with an organic, internal phase containing poly(lactic acid) stabilized by chitin/cellulose nanofibers and a continuous, crosslinkable hydrogel containing cellulose nanofibers and any of given solid particles. The shear during ink extrusion through nozzles of low surface energy facilitates the generation of the enveloped structures by fast and spontaneous phase separation of the emulgel. The skin-bearing architectures enable control of mass transport as a novel configuration for cargo release. As a demonstration, we loaded a hydrophilic molecule in the hydrogel, which was released on demand through the core and skin, enabling regulation of diffusion and permeation phenomena. Such 3D-printed functional material allows independent control of strength owing to the hierarchical construction. The new method of fabrication is proposed as a simple way to achieve protection, regulation and sensation, taking the example of the functions of skins and cuticles, which are ubiquitous in nature.

1. Introduction

The skin in mammals, as one of the most important organs, and the cuticle in plants, designed by nature for protection, are critical for survival, adaptation and function.[1] They also regulate the interactions with the surrounding environment,[2] e.g., by channeling connections with the inner microstructure.[3] Such spatial confinement preserves morphology and structure, which is hierarchical to achieve protection-regulation (e.g., bark)[4] and protection-regulation-sensation (e.g., human skin).[5] From the biomimicry point of view, functionalities including controlled permeation,[6] insulation,[7] and mechanical strength[8] arise from layered outer/inner structures, which are relevant to a wide range of man-made constructions used in biomedicine, separation and others. Materials that exhibit hierarchically layered structures have been shown to surpass their counterparts, for instance, in self-adaptation and property adjustment.[9] Bio-inspired layered stiff plate/soft matrix composite materials have been reported,[10] but more universal, complex systems that use layered structures have been studied very scarcely, mainly owing to the challenges posed by their synthesis.

3D printing allows a high level of topological complexity while ensuring robust custom-shaped structures.[11] Among various 3D printing techniques, extrusion-based direct ink writing (DIW) enables programmable, precise layer-by-layer assemblies in three dimensions.[12] The inks suitable for the DIW must exhibit shear-thinning to enable efficient flow through the nozzles but demand fast recovery into objects with a sufficiently high yield stress and storage modulus, to ensure shape retention and distortion-free geometries.[13] Unlike lithography or laser-based polymerization, DIW materializes sophisticated microfabrication for a wide range of materials, such as hydrogel, emulsions, and foams.[14] To this end, DIW can be used to integrate the functions of materials across multiple length-scales, a prerequisite for the construction of hierarchical organizations. This usually implies multiple stage-wise processes since single-step, simultaneous fabrication of outer/inner construct *via* DIW remains intractable, given the requirement for the inks to self-separate upon printing. Moreover, the formation of

spatially-resolved and gradient structures often requires multiple inks that are printed either simultaneously or sequentially, namely, multi-material printing.[15] The latter process usually alters the fidelity and increases operational complexity. The development of all-in-one ink is therefore paramount to facilitate the deployment of hierarchically layered constructs.

To tackle the presented challenges, we propose multi-component materials consisting of immiscible but metastable phases given the possibility of spontaneous phase-separation.[16] For example, we have recently reported on multiphase emulsions to generate complex structures *via* 3D printing using DIW.[17] While our initial aim was to gain control on the properties of the emulsion ink by changing the formulation (e.g., emulsion morphology), the results hinted to the possibility of achieving hierarchical architectures.[18] However, this depends on the ability to engineer phase-separation to achieve high fidelity without compromising the required balance between ink composition and printability.[19] In line with this effort, we noted that the absence of a solid support in the aqueous phase of the emulsion prevented phase separation;[20] otherwise, such phenomenon could be enhanced by the incorporation of a hydrophilic component that is miscible with the aqueous phase to solidify the emulsions prior to printing.[21]

Hence, here we propose a two-phase emulgel ink comprising an oil-in-water Pickering emulsion. More specifically, the dispersed phase contains poly(lactic acid) (PLA) while the continuous phase is a physical crosslinkable hydrogel loaded with silica particles. An alkaline solution (ammonia) is titrated to solidify the hydrogel phase and generate the printable emulgels (**Figure 1a**). Such emulgels are easily transformed into layered materials *via* spontaneous phase-separation upon deposition during DIW printing, representing a one-step process to create struts or filaments with a core covered by a coating or skin layer.

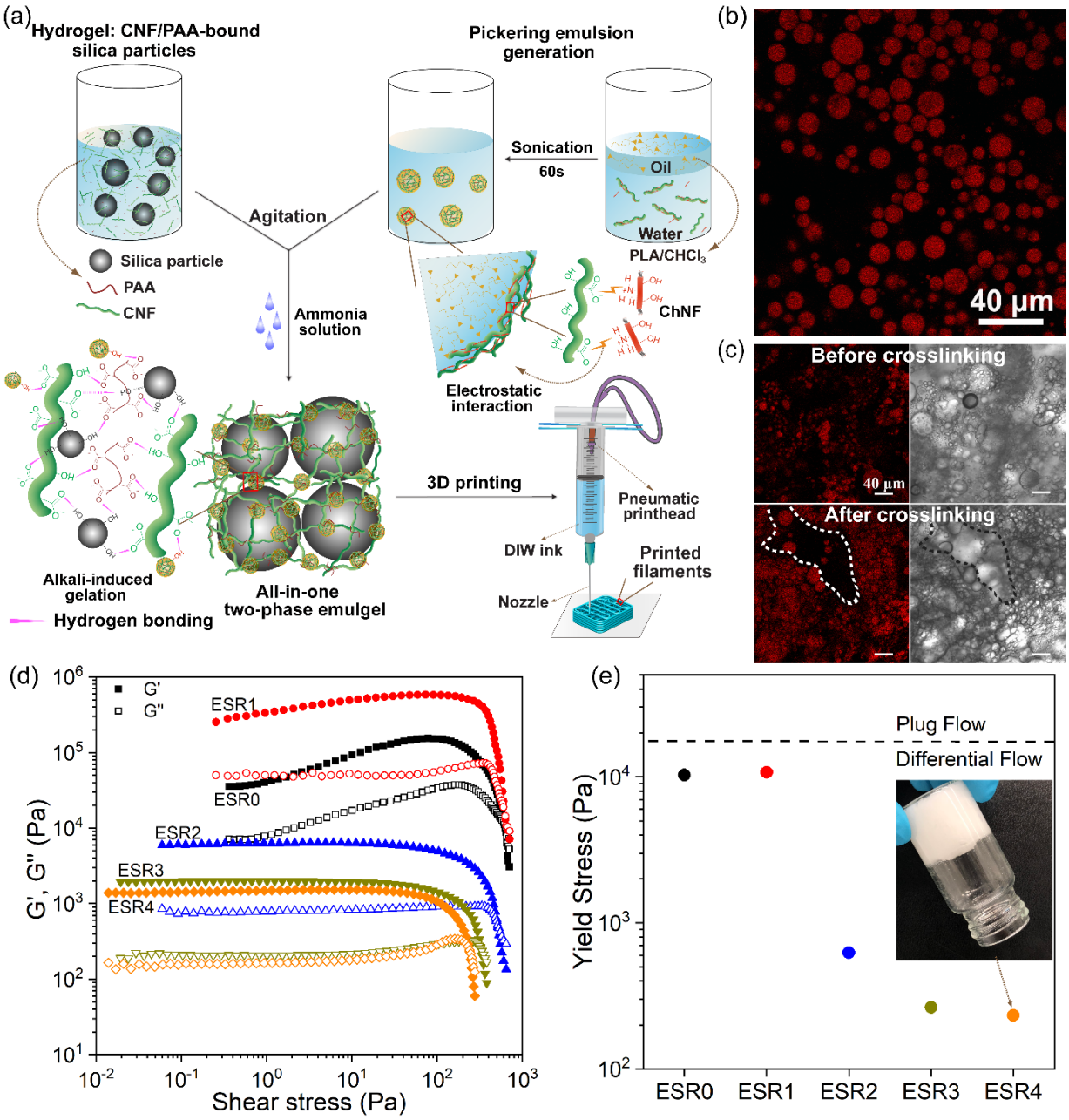

Figure 1. (a) Schematic illustration (not to scale) of the fabrication of all-in-one, two-phase emulgels. (b) Confocal image of a PLA/$CHCl_3$-in-water Pickering emulsion stabilized by nanofibrils isolated from cellulose (CNF) and chitin (ChNF), as shown in (a). (c) Confocal and bright field images of two-phase emulgels before (upper) and after (bottom) alkali-induced gelation. Sample ESR4 was used for imaging. The dashed line highlights a region depleted of droplets after gelation. The scale bar is 40 μm for (b) and (c). (d) Oscillatory rheology of the emulgels with increasing emulsion loadings (ESR0 to ESR4). ESR0 indicates a system with no emulsion present. The emulsion-to-silica particle ratio in ESR1 to ESR4 correspond to 19:32, 29:22, 39:12, and 45:6, respectively. (e) Shear yield stress of the emulgels, following the same color code used in (d). The added dashed line denotes the transition from differential to plug flow. The photo insert displays the ESR4 system in an inverted vial (2.5 cm diameter).

2. Results and Discussion

2.1. Structure and rheological properties of two-phase emulgels

The effect of emulgel composition was studied by varying the emulsion-to-hydrogel ratio, more precisely, the emulsion-to-silica particle ratio (thereafter referred to as ESR#, where # is a number between 0 and 4, as shown in **Table 1**). The choice of Pickering emulsion stems from the fact that colloidal particles can adsorb irreversibly at the oil/water interface, generating an interfacial barrier that limits droplet coalescence and endows emulsions with superior stability compared to those produced with surfactants.[22] We have previously shown that a mixture of anionic cellulose nanofibrils (CNF) and cationic chitin nanofibers (ChNF) is highly efficient in stabilizing oil-in-water emulsions (e.g., PLA/$CHCl_3$-in-water Pickering emulsions).[17,23] In such systems, cooperative adsorption and network formation at the oil/water interfaces are the main reasons for achieving high emulsion stability. Here, PLA/$CHCl_3$ droplets with sizes of approximately 8 μm were well dispersed in the aqueous phase, which contained CNF and ChNF at low concentration (0.5 wt%), ensuring a homogeneous emulsion for emulgel preparation (**Figure 1b** and **Figure S2**, Supporting Information). The high stability of PLA droplets results from their high surface charge (*ca.* +60 mV, **Figure S1c**, Supporting Information), as well as the strong steric hindrance originated by the fibrillar network formed around the droplets (**Figure S2**, Supporting Information). No free CNF nor ChNF are present in the continuous, aqueous phase, as confirmed by fluorescence imaging (staining CNF/ChNF by Calcofluor white, **Figure S2**, middle image, Supporting Information). Moreover, the calculated surface coverage of the stabilizer on the PLA droplets is much less than that corresponding to full coverage (see **Supporting Information**). Thus, the aqueous phase of the emulsion took no part in the crosslinking that was used to obtain post-crosslinked emulgels.

Table 1. Composition of the all-in-one two-phase emulgels used for DIW printing

Sample	Emulsion (wt%)	Silica (wt%)	PAA/CNF[a)] (wt%)	Dry solid content (wt%)[b)]
ESR1	19	32	49	33.2
ESR2	29	22	49	23.5
ESR3	39	12	49	14.6
ESR4	45	6	49	7.8
ESR0[c)]	0	32	68	33.1
ESR01	0	12	88	13.5
ESR02	0	6	94	7.6

[a)]The ratio for PAA to CNF was 2:1 in all samples; [b)]Dry solid content corresponds to the mass of the printed structures after drying; [c)]ESR0 indicates that no emulsion was added to the ink.

The adoption of silica-loaded hydrogel was inspired from our previous report wherein mechanically strong materials were produced after drying suspensions containing silica microparticles and CNF.[24] Herein, the hydrogel was formed by the addition of poly(acrylic acid) (PAA) that is crosslinked in the presence of ammonia solution.[25] Subsequently, Pickering emulsions and hydrogels were mixed to generate emulgel precursors, which could be solidified upon PAA crosslinking (an illustration of the system is included in **Figure 1a**). Before titrating ammonia solution, PLA droplets in the emulsion were homogeneously mixed with silica particles within the hydrogel (**Figure 1c**, top, and **Figure S3a**, Supporting information). After crosslinking, however, silica particles strongly interacted with CNF *via* PAA-induced inter-particle hydrogen bonding, making PLA droplets to diffuse out and to envelope the solid particles (**Figure 1c**, bottom, and **Figure S3b**, Supporting Information), as also illustrated in **Figure 1a**. The weak interaction between PLA droplets and silica particles arises from the fact that CNF is not available on the surface of the droplets, which otherwise would produce CNF-silica-PAA networks. In fact, most of the CNF on the droplets interacts electrostatically with ChNF to enable higher stabilization ability. Such segregated structure within the emulgel, which is formed upon crosslinking, facilitates separation of the ink into two phases during printing; however, macroscopically, phase separation is not apparent in the crosslinked emulgel (**Figure 1e**, inset).

The printability of the emulgels is determined by their rheological properties: see **Figure 1d** and Supporting Information **Figure S4** for the rheological behavior of the emulgels at different emulsion-to-silica particle ratios. All the emulgels underwent pronounced shear thinning and displayed similar flow profiles; the apparent viscosity decreased, by several orders of magnitude, with increasing the shear rate from 10^{-2} to 10^{2} s^{-1} (values typically applied in DIW to ensure flow through the deposition nozzle) (**Figure S4**, Supporting Information). Oscillatory rheological measurements at low strain indicated that the storage modulus (*G'*) of all the emulgel inks dominated at lower shear stresses whereas the loss modulus (*G''*) became more relevant at high shear stresses after crossing the yield stress point (τ_y, $G' = G''$) of the respective emulgel (**Figure 1d**). This behavior is attributed to the significant post-crosslinking effect between CNF, PAA and silica particles, even at the lowest silica loading (ESR4). On the other hand, **Figure 1d** indicates that the *G'* and τ_y decreased with increasing loading of the emulsions (namely decreasing the amount of silica particles, ESR1 to ESR4). This can be attributed to the less solid-like nature of the emulgels at high emulsion content. It should be noted that the *G'* and τ_y of the silica particle-based hydrogel (no emulsion, ESR0) were slightly lower than those of ESR1. Thus, although both samples contained identical amounts of silica particles (**Table 1**), there is indication that the addition of a small amount of emulsion promoted a stronger gelation.

We note that even if the rheological properties are appropriate for DIW, a high τ_y and apparent viscosity of the emulgel may generate a high printing pressure, for example, if the maximum yield stress (τ_{max}) generated within the nozzle is not sufficient to overcome the τ_y of the emulgels. In such case, plug flow occurs and prevents continuous printing. To determine if this is the case of the present inks, we calculated the radial τ within the deposition nozzle during printing, equation (1):[13a]

$$\tau = \frac{\Delta P}{2L} r \qquad (1)$$

where ΔP is the maximum pressure applied at the nozzle, r is the radial position from the center of the nozzle, and L is the nozzle length. Using $\Delta P = 7 \times 10^5$ Pa, $r = 6.3 \times 10^{-4}$ m, and $L = 1.27 \times 10^{-2}$ m, the calculated τ_{max} for the nozzle is 1.7×10^5 Pa. Comparing the τ_y of the emulgels and τ_{max} within the printer nozzle (dotted line in **Figure 1e**), it was determined that $\tau_y < \tau_{max}$ and therefore no plug flow was expected for any of the two-phase emulgels used as DIW inks. Overall, the rheological results highlight the ability of the emulgel inks to maintain their shape upon printing.

2.2 Printing 3D structures from two-phase emulgels

2.2.1. Skin-bearing structures printed from emulgels

As will be shown, the emulgels used in DIW allow the design of hierarchically layered architectures with functions that can be independently controlled at the micro- and milli-meter scale. By using a 0.63-mm-diameter nozzle, layered cubic grids were easily created. As an illustration, ESR2 emulgel was extruded through the nozzle and underwent rapid solidification after ceasing the shear, enabling continuous DIW printing (**Video S1**, Supporting Information). Upon freeze-drying, the shape and size of the original designs were fully retained, with no apparent collapse, deformation nor shrinkage. Moreover, the boundary between the stacked layers were visible and indicated 3D objects with a fine resolution at the micrometer scale (**Figure S5b**, Supporting Information). As a control, a grid composed of pure silica-filled hydrogel (with no emulsion, ESR0) was printed. No observable, macroscopic difference existed in comparison with the grid produced from the emulgel of similar rheology, e.g., ESR3 (**Figure S5a**, Supporting Information).

However, at the microscopic level, the grids printed from different emulgels exhibited remarkable differences (**Figure 2**). For a neat hydrogel ink (ESR0), a homogeneous arrangement of particles and fibrils was observed across the structure of the printed filaments or struts (**Figure 2a$_1$**). This is owing to the ability of CNF/PAA to bind strongly with silica

particles after crosslinking (**Figure 2a$_2$**).[24] The cross-section of ESR0 indicates filaments comprising well-packed networks of silica particles (**Figure S6a**, Supporting Information). In the presence of the emulsion phase and with its increased content, the emulgels formed filaments that were enveloped by a skin or outer layer, even at low emulsion loading (ESR1, **Figure 2b$_1$**). The skin coverage on the filaments increased with increasing the emulsion fraction in the emulgel, and full coverage took place at the highest emulsion content (ESR4, **Figure 2e$_1$**). The surface morphology of the skin transformed from large pores or cracks, uneven mesopores, to dense surface-containing nanopores (**Figure 2b$_1$-e$_1$**). These results indicate that the formation and morphology of the skin correlate with the emulsion fraction in the emulgels (**Table 1**). Interestingly, the skin formed separately from the core of the filaments (**Figure 2b$_2$ and c$_2$**). Such phase separation upon solidification was confirmed by the cross-section images of filaments ESR2 and ESR4 obtained using scanning electron microscopy (SEM) (see high magnification image of ESR4, **Figure S6b-d**, Supporting Information). The cross-section also indicates the possibility of adjusting the thickness of the skin, depending on the emulsion loading. We note that neither the emulsion droplet size, nor PLA loading level, had an influence on the formation of the skin (see **Figure S7** and **S8** in Supporting Information and discussion). Overall, the results demonstrate two-phase emulgels for a one-step fabrication of structures *via* DIW printing producing architectures with a core protected by a skin.

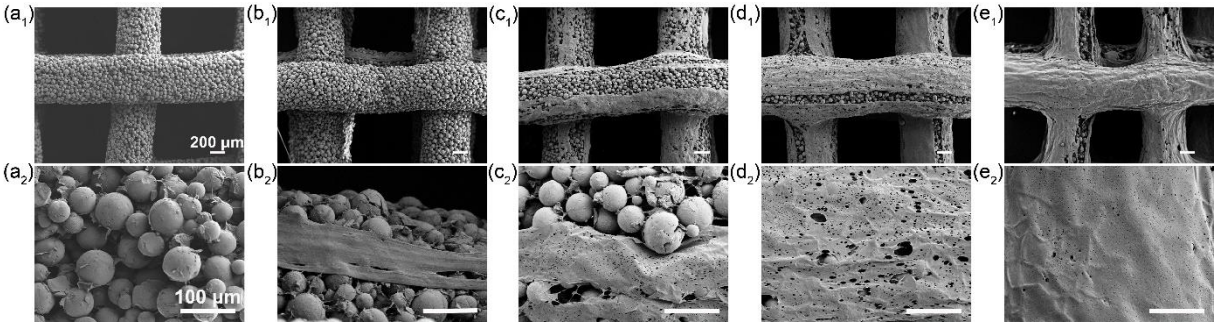

Figure 2. Scanning electron microscopy (SEM) images of the printed structures (crossing in the grids are shown) prepared from two-phase emulgels: (a_1, a_2) ESR0, (b_1, b_2) ESR1, (c_1, c_2) ESR2, (d_1, d_2) ESR3, and (e_1, e_2) ESR4. The needle size was 0.63 mm for all the samples. All

the grids were freeze-dried at least 2 days before imaging. The scale bar is 200 μm for (a_1) to (e_1), and 100 μm for (a_2) to (e_2).

Additional emulgels were formulated with hydrogels containing solid particles different than silica, namely, nanoclays, fumed silica, iron (II, III) oxide, and hydroxyapatite. All these particles are commercially available, and reported to have distinctive physicochemical properties (see **Table S1** in Supporting Information for the refractive index and zeta potential). Such systems were successfully printed into structures similar to those discussed before (**Figure S9**, Supporting Information). The universality of the proposed method owes to the fact that the composition of each phase depends only on their individual components, that is, a broad range of solid particles, regardless their size, shape, hydrophilicity, and surface properties, could be used to prepare suitable hydrogels. It should be emphasized that the surface charge (type and value) of the particles showed no significant effect on the formation of the skin although the mixture of CNF/PAA was negatively charged (**Table S1**, Supporting Information). We also replaced the PLA encapsulated in the emulsion with polystyrene (PS). As was the case of the hydrogel, the ink was successfully applied provided an emulsion was formed. In the above experiments we used a fixed emulsion-to-particle ratio (45:6, as in ESR4) and although the properties of supporting particles and polymer were different, the printed grids reflected the intended design (**Figure S7a_1-e_1**, Supporting Information). Moreover, SEM images of the grids confirmed skin structures fully covering the surface of the filaments (**Figure S9a_2-e_2**, Supporting Information, similar to the case of ESR4, **Figure 2e**). Importantly, the microstructural details did depend on the particles used (**Figure S9a_3-e_3**, Supporting Information), which expand the property space for the emulgels as universal inks toward hierarchical architectures and for given applications.

2.2.2. Formation mechanism of skin-bearing structures upon printing

We thoroughly investigated the mechanism underlying skin formation (**Figure 3**). In the emulgel, the PLA was dissolved in a nonpolar solvent, which resulted in phase separation of PLA droplets from the hydrogel, owing to the difference in polarity or hydrophilicity.[19,26] The shear force applied during printing induced phase separation,[27] but this may not occur spontaneously, depending on the affinity between the phases.[28] On the other hand, it has been shown that in multiphase systems segregation of a hydrophobic phase or component towards hydrophobic surfaces occurs readily.[29] Given that a hydrophobic needle (polypropylene) was used for printing, it is reasonable to assume that the skin is principally composed of the hydrophobic component of the emulsion, wherein the shear upon printing and segregation promoted phase separation and subsequent surface minimization (**Figure 3a**). Additionally, as PLA was emulsified by the mixture of CNF and ChNF, outward transport of PLA-based droplets was facilitated by the pre-separated internal structure of the emulgels upon crosslinking (**Figure 1c**). The hydrophobic N-acetyl groups in ChNF facilitated interactions with PLA droplets and the inner surface of the needle.[23] On the other hand, the evaporation of chloroform within PLA droplets upon printing might create a convective flow along with the hydrophobic inner surface of the needle, which may further increase the wettability of PLA droplets on the inner surface, thereby rendering a more effective phase separation. We selectively dissolved PLA from the grids using chloroform to confirm the composition of the skin. SEM images of the structure showed no residual skin on the filament surface; however, bound particles were still evident, demonstrating that the skin contained the nonpolar phase inside the emulsion, in this case PLA (**Figure 3b and c**). Particularly, after washing, some PLA spheres were trapped in the nanoclay layers, as shown in the insert of **Figure 3c**, which may be caused by the tight stacking of nanoclay layers. This result clearly demonstrates that phase separation of PLA droplets occurred during printing, leading to skin formation.

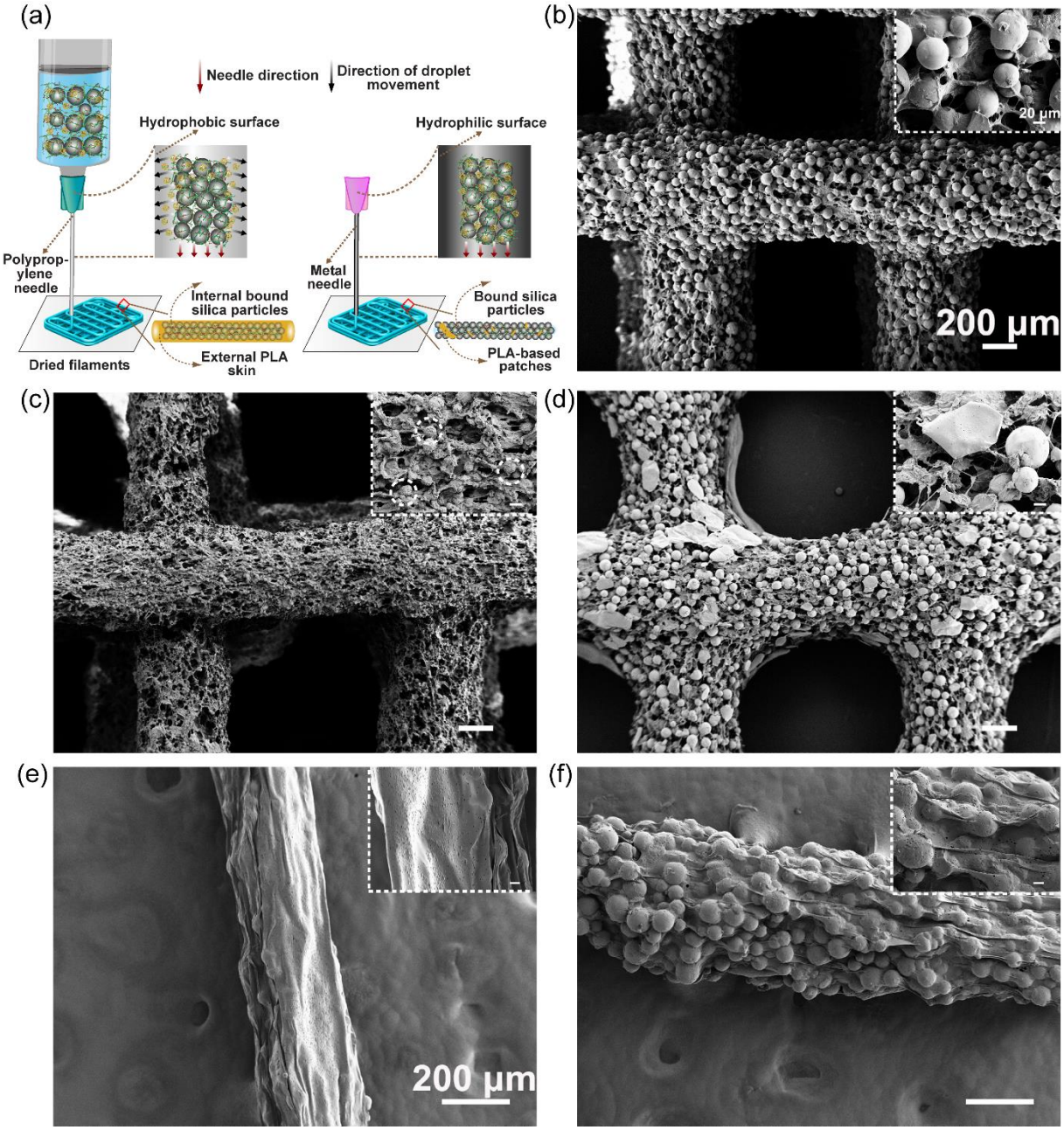

Figure 3. (a) Schematic illustration (not to scale) of the skin formation mechanism upon printing. Surface morphology of printed structures including (b) silica particle and (c) nanoclay after removing PLA by immersing in chloroform. The ratio of emulsion-to-supporting material is 45:6 for both samples. The dash circles in (c) indicate PLA spheres trapped in the nanoclay layers. (d) Microstructure of the grid printed through a metal needle (ESR4). The scale bar is 200 μm for (b) to (d). Microstructure of the filaments printed from ESR4 after drying at (e) room temperature and (f) 85 ℃ oven. The scale bar is 200 μm for (e) and (f). The inserts in (b) to (f) are high magnification images, and the scale bar is 20 μm.

To confirm the role of hydrophobic interaction in phase separation at the needle surface, a hydrophilic needle (0.63 mm, made from passivated stainless steel) was used for emulgel printing (ESR4, **Figure 3a**). SEM images of the grid printed through hydrophilic metal needle was remarkably different compared to those produced from hydrophobic needle (**Figure 3d**). Particularly, no continuous skin was formed, and the dimension of PLA-based patches was quite wide, implying that the phase separation within the emulgel was either weak or partial. Additional evidence supporting poor phase separation within the later system is the observation of fragmented PLA films trapped in the inner regions of the filaments (**Figure 3d**, inset). The surface wettability of both needle types by the emulsions was evaluated by measuring the contact angle. A poor surface wettability was noted for the hydrophilic metal needle (**Figure S10**, Supporting Information), which highlights the role in phase separation of the interactions between the emulsion phase and the inner surface of the needle. It is worth noticing that the filaments printed from metal needles fused in the grid structure (no boundary was presented). This did not occur for skin-bearing filaments produced from hydrophobic needles, further highlighting the ability to produce skins in such condition and to synthesize hierarchical architectures with micrometer-scale fidelity.

Knowing the origin of the skin, the next question is if the skin is formed upon drying. To resolve this issue, we investigated different drying methods: SEM images of filaments dried at room temperature and at 85 ºC showed similar skin structures compared to those produced by freeze-drying (**Figure 3e and f**). Under room temperature, the skin was rougher and uneven while oven drying led to a significant shrinkage of the skin, which closely wrapped around the filament, likely due to a faster water evaporation rate. The accumulation of hydrophobic PLA droplets that separated out upon printing is energetically unfavorable, considering the increased interfacial energy and the minimization of surface area of the separated domains.[12b,30] This minimization induced the coalescence of PLA droplets to form large domains that separated from the filament core; upon chloroform and water evaporation, a solid skin consisting of PLA

and CNF/ChNF was formed through the diffusion and entanglement of PLA chains and the network of fibrillar nanoparticles.[31] All in all, there is evidence that the skin formation did not depend on the drying process.

2.3 Properties of printed skin-bearing constructs

2.3.1. High printing fidelity

The fidelity of printed constructs reflects the printability of the emulgels. Herein, however, skin formation brings an extra level of control over such fidelity, as shown in structures printed even at low silica content (ESR3 and ESR4, **Figure 2d and e**). For instance, in the absence of emulsion phase, high-fidelity filaments were printed from the hydrogels provided that a high silica particle loading was used (32 wt%, **Figure 2a**). At low particle loading (<12 %), however, the filaments fused together after drying, with no clear boundaries (**Figure S11a** and **b**, Supporting Information). As a result, the skin structures prevented the merging or fusion of the different layers upon printing and drying. Notably, the mechanical strength of the printed grids increased with the skin coverage (**Figure S12**, Supporting Information). In order to show the high fidelity of objects bearing skin at the millimeter scale, we used emulgel ink ESR4 to print grids with needles of different diameters (**Figure 4a-d** and **Video S2**, Supporting Information). All the grids maintained the original dimensions and clear grids, which were not possible by DIW printing of low solid inks.[16] Moreover, the skin was formed regardless of the needle diameter (**Figure 4e** and **f**), demonstrating the universality of skin structure under different printing conditions. Therefore, the presence of a spatially segregated skin enveloping the filaments have a protective effect, maintaining the morphological integrity and even enhancing the mechanical strength of the grids, both at the micro- and millimeter scales. In this context, these effects are taken as mimics to those found in skins and cuticles in nature.

The macroscopic shape of 3D printed objects is also critical for any application. A two-phase emulgel was used to produce complex architectures at the millimeter scale by printing a human dental replica using hydroxyapatite as solid filler (**Figure 4g**), which clearly retained

details as designed. Letters were also printed to demonstrate the ability to produce high curvatures and round structures (**Figure 4h**). Moreover, the macroscopic layers produced during printing were clearly identified from the enlarged images, indicating the ability of emulgels to create objects showing high levels of geometrical complexity, at the millimeter scale (**Figure S13**, Supporting Information). Overall, objects bearing skin structures printed from emulgels exhibit high fidelity at relatively low solid content.

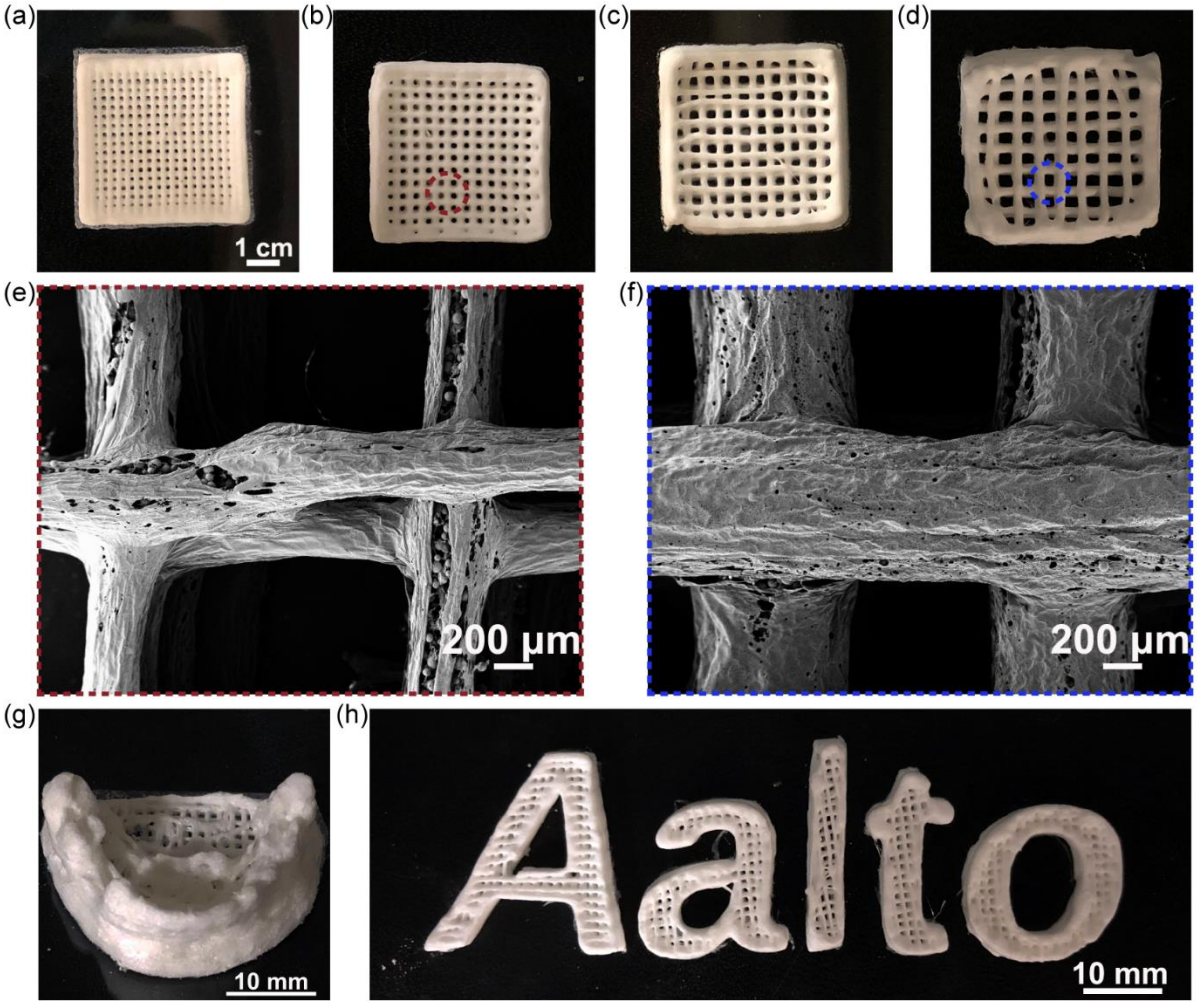

Figure 4. Top view of cubic grids printed with ESR4 ink using a needle size of (a) 0.25, (b) 0.41, (c) 0.63, and (d) 0.84 mm. The scale bar is 1 cm for (a) to (d). SEM images of the grids printed by using (e) 0.41 and (f) 0.84 mm needle. The scale bar is 200 µm for (e) and (f). Top view of the 3D-printed model of (g) a human dental and (h) the letters Aalto. In (g) and (h), hydroxyapatite and silica particles were used as the solid supporting materials, respectively. The emulsion-to-supporting material ratio was 45:6 for both samples. The scale bar is 10 mm for (a) and (b). All the printed objects were freeze-dried at least 2 days before characterization.

2.3.2. Controlled release of hydrophilic cargo

An outer layer in the 3D printed structures is expected to contribute to enhanced protection and mechanical performance. It also facilitates control on the interaction with the surrounding medium, which is an important function for skin mimicry. A point in case with relevance to drug delivery is the effect of the skin in channeling cargos between the core and the surrounding medium (**Figure 5**). We assessed this feature by testing the release of a hydrophilic compound (sodium salicylate, SAL) that was encapsulated in the hydrogel. Owing to its hydrophilicity, SAL is expected to be retained in the hydrogel phase during printing. Here, we utilized the hydrophobic skin to tune the permeability and diffusivity of SAL to the surrounding medium. The drug payload was fixed at 5 wt% of the final dry mass of the grids (**Table 1**); no alterations in grid microstructure was observed (**Figure S14**, Supporting Information). In order to verify the effect of the skin, we determined the drug release profiles for various grids, e.g., those prepared from ESR0 (no skin) to ESR4 (fully-covering, thick skin). All the release profiles were similar in shape but presented distinctive release rates, with an initial burst release followed by a slow one (**Figure 5a**). Within the burst release time range, a remarkable effect was enabled by the skin: an increased skin coverage gradually slowed down the release rates (**Figure 5a**$_2$).

The mechanism for drug release was elucidated by using kinetic models that describe diffusion through pores or by polymer relaxation, both of which fitted reasonably well the drug release profiles but indicated an anomalous cargo release (**Table S2**, Supporting Information).[32] Thus, the experimental data and the kinetics describing the mechanism of drug release indicates the synergistic effects that arise from the combination of a pore matrix and a polymeric shell or skin. The Peppas-Sahlin model was selected to describe the individual contribution of each mechanism (diffusion through pores and relaxation). By plotting the release coefficients for diffusion (k_1) and relaxation (k_2) as a function of the skin, a reverse scaling of the coefficients was observed (**Figure 5b**). With the increased skin coverage, k_2 played a more prominent role, which is attributed to more hydrophobic and less porous PLA

layer that acted as a barrier hindering spontaneous release from the grid. As observed in the **Figure 5b**, k_2 is an order of magnitude lower than k_1, which results in slower drug diffusion through the relaxed polymer when compared to the porous, inner filaments. Particularly, a fine tuning of the diffusion and permeability kinetics is achieved by changing the composition of the inner particles or the skin, as demonstrated for different silica particle loadings in the hydrogel (**Figure S15**, Supporting Information). From these observations, the mechanism underlying the controlled drug release is illustrated in **Figure 5c**. The single circular cross-section used in this visualization is meant to represent the release rate of a single component of the printed objects that were in fact built from more complex architectures (**Figure 2 and 4**). Here, the diffusion along the length is negligible compared to that in the radial direction. In summary, the drug release tests for skin-bearing grids demonstrates the capability of the skin to controllably regulate the channeling of the inner component to the outer medium, which offers a great potential for applications in advanced functional devices.

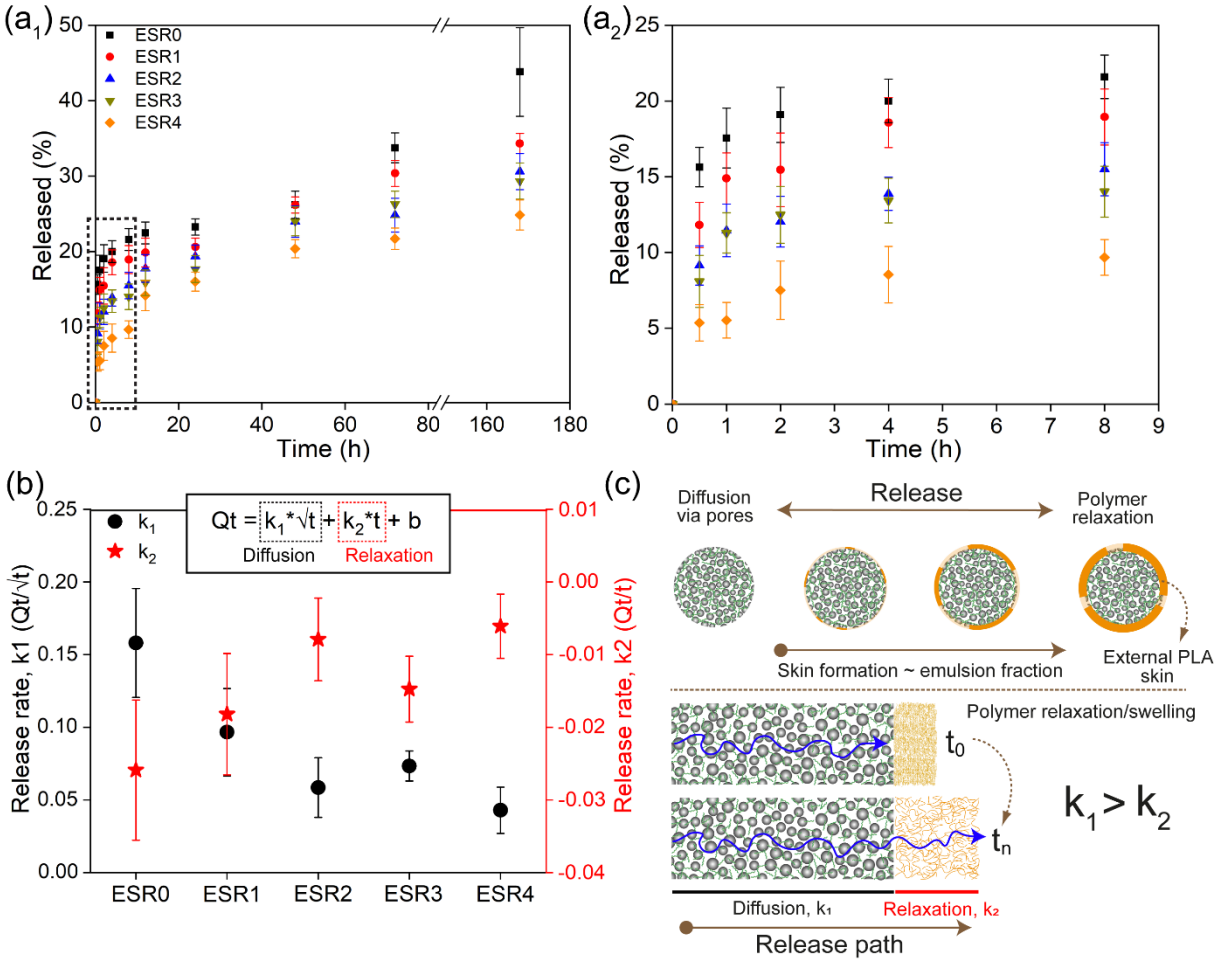

Figure 5. (a_1) Full and (a_2) initial release profiles sodium salicylate in aqueous media after loading in the hydrogel prior to mixing with the Pickering emulsion followed by printing and drying. The grids (cubic in shape) were printed from the ESR4 ink using the 0.63-mm needle. (b) Release rate coefficients (k_1 and k_2) obtained after linearization of the experimental data using the Peppas-Sahlin model. (c) Schematic illustration (not to scale) of the drug release as affected by the skin surrounding the supporting silica particles.

3. Conclusions

We propose two-phase emulgel systems for one-step fabrication of 3D-printed, skin-bearing architectures. DIW printing of the emulgels enabled precise phase-separated structures, which cannot be achieved through any other mono-component ink. Moreover, the universality of the emulgel concept was demonstrated for diverse types of components, allowing the tailoring of hierarchical microstructures that are suited to different demands. The generation of skin structures around the filaments occurred from spontaneous phase separation of the emulgel, which was enhanced by shearing upon printing and depended on the surface energy of the

surface of the printing nozzle. The extrusion of emulgels by DIW allowed for the independent control of robustness and functionality of the skin-bearing objects at the milli- and micro-meter scales. The skin on the filaments was used not only as a protection to keep the integrity of the hierarchical structure and to improve the mechanical strength, but also to tune the diffusion and permeability of cargos, enabling the regulation of transport and channeling to the outer environment. It is anticipated that the proposed emulgel strategy for DIW printing will open the possibility to engineer complex hierarchical constructs. On the ground of biomimicry from animal skins and plant cuticles, protection, regulation and sensation are some of the possibilities for this new generation 3D-printed architectures.

4. Experimental Section

Materials: Cellulose nanofibers (CNF) were obtained from never-dried, bleached, and fines-free sulfite hardwood fibers *via* passing through a microfluidizer (M110P, Microfluidics Int. Co., Newton, MA), as described previously.[19] Chitin nanofibers (ChNF) were extracted from crabs following a series steps of washing, decolorizing, deacetylation, and ultra-sonication, according to the procedures described previously.[24] Polylactide (PLA, 6060D, M_w=191,000) was kindly provided by Nature Works, United States. Chloroform ($CHCl_3$), poly(acrylic acid) (PAA, M_w=4,000,000), polystyrene, silica gel particles (40-75 μm), fumed silica (0.2-0.3 μm), nanoclay ($\leq$ 25 μm, hydrophilic bentonite), iron (II, III) oxide ($<$5 μm, 95%), and hydroxyapatite (2.5 μm, ≥100 m^2/g) were purchased from Sigma-Aldrich (Helsinki, Finland) and used as received.

Preparation of all-in-one two-phase emulgel as ink for DIW: Pickering emulsions were prepared similarly as previous studies.[23b,24] Suspensions of CNF and ChNF were both diluted to 0.5 wt% and then mixed thoroughly to obtain homogeneous suspension (**Figure S1a**, Supporting Information). 10 ml of PLA/$CHCl_3$ (4 wt%) was added into 10 ml of CNF/ChNF suspension and pre-emulsified by hand-shaking, and then fine emulsions were obtained *via*

sonicating for 60 s under 40% power level with alternating on-off cycles (3 s-2 s, respectively) (Titanium tip sonicator, Sonifier 450, Branson Ultrasonics Co., Danbury, CT, USA).

The hydrogel was prepared by mixing silica particles, CNF (1 wt%), and PAA (2 wt%) at designed mass combinations wherein the PAA to CNF ratio was 2:1. For emulgel preparation, emulsions were added into the hydrogel under vigorous blending. The emulsion/hydrogel precursor was placed at room temperature for 30 min prior to crosslinking. Several drops of ammonia solution were injected into the precursor with thorough mixing to generate emulgel. The emulgel obtained was placed at room temperature for at least 2 h to enable sufficient crosslinking.

To test the universality of emulgel system, nanoclay, fumed silica, iron, and hydroxyapatite were used to replace silica particles under the same approach for preparing the hydrogel. Polystyrene was used to replace PLA with the same procedure to produce Pickering emulsion.

Morphology of emulgel: The morphology of emulsion/hydrogel precursors and post-crosslinked emulgels was characterized by confocal laser scanning microscope (CLSM) with a 40× oil immersion objective lens (Leica DMRXE, Leica, Germany) at transmittance and fluorescent modes. The oil phase of the emulsion was dyed with Nile red solution (1 mg/mL ethanol) prior to emulsion preparation. The sample was placed on a microscope slide and covered with a glass coverslip before observation. The excitation and emission spectrum for Nile red are 488 and 539 nm, respectively.

Rheological measurement: Rheological behavior of the emulgels was measured with a rheometer (MCR 302, Anton Paar, Germany) using parallel plates (PP25) with a gap fixed at 0.5 mm. All samples were pre-sheared at 10 s^{-1}. The apparent shear viscosity was monitored by increasing the shear rate from 10^{-2} to 10^{2} s^{-1}. Oscillatory measurements were carried out at a constant frequency of 1 Hz and increasing stress from 10^{-2} to 10^{3} Pa. All measurements were performed at 25 °C.

3D printing of emulgel inks: 3D bioprinter (BIO X, CELLINK, Sweden) with pneumatic functioning printing head was used to print the emulgels. The device utilized 3 ml pneumatic syringe provided by CELLINK and sterile blunt needles (plastic or metal, Drifton, Denmark). The nozzle size of the needle was 0.25, 0.41, 0.63, and 0.84 mm. Cubic grid grids (20 mm × 20 mm × 5 mm) and specially designed shapes (dental and letters) were printed on the plastic Petri dish, for which the grids had rectilinear infill pattern and 30% infill density. Based on primary optimization, the moving speed of the printhead was 8 mm/s, the extrusion speed was 0.012 mm/s, and the extrusion pressure was controlled in the range of 20-200 kPa. After printing, the samples were freeze-dried at least 2 days before characterization. For comparing different drying methods, the printed samples were dried by placing at room temperature or 85 ℃ oven.

Characterization of the grids: The microstructure of the filaments in the grids was observed by scanning electron microscopy (SEM, Zeiss Sigma VP, German) operated under vacuum and at an accelerated voltage of 2 kV. The structure of cross-section was revealed from clean knife cuts. The samples were sputter-coated with platinum before imaging.

Drug release test: The drug was incorporated in the grids prior to printing. For this, 5 wt% of sodium salicylate related to the dry mass of the final object was dissolved in the hydrogel phase. A calibration curve in the range of 0.01 to 0.1 mg/mL for the determination of the drug concentration in water was built using the linear correlation between absorption at 296 nm and concentration (**Figure S15**, Supporting Information). The release study was carried out at 25 ℃, using Milli-Q water containing 0.5 w/v% NaCl as releasing medium (pH = 7). The grids (of known mass) were individually placed in the bottom of the separated flasks, which directly contacted the release medium (known volume). Aliquots of the medium were withdrawn at given times for UV spectra acquisition. Before sampling the flask was agitated for homogenization of the dissolved drug. The shape of all the grids loaded with drugs was kept unchanged during test. The release profiles were acquired with triplicates.

Supporting Information

Supporting Information is available from the Wiley Online Library or from the author.

Acknowledgements

We acknowledge funding from the European Research Council (ERC) under the European Union's Horizon 2020 research and innovation programme (ERC Advanced Grant agreement No 788489, "BioElCell"). This work made use of the facilities of Aalto University's Nanomicroscopy Center.

Received: ((will be filled in by the editorial staff))
Revised: ((will be filled in by the editorial staff))
Published online: ((will be filled in by the editorial staff))

References

[1] a) E. A. Grice, H. H. Kong, S. Conlan, C. B. Deming, J. Davis, A. C. Young, NISC Comparative Sequencing Program, G. G. Bouffard, R. W. Blakesley, P. R. Murray, E. D. Green, M. L. Turner, J. A. Segre, *Science* **2009**, *324*, 1190; b) P. H. Raven, R. F. Evert, S. E. Eichorn, *Biology of plants*, W.H. Freeman and Co., New York, USA, **2005**; c) B. J. F. Bruet, J. H. Song, M. C. Boyce, C. Ortiz, *Nat. Mater.* **2008**, *7*, 748.

[2] M. Sára, U. B. Sleytr, *J. Bacteriol.*, **2000**, *182*, 859.

[3] a) E.A. Grice, J. A. Segre, *Nat. Rev. Microbiol.* **2011**, *9*, 244; b) F. J. Vernerey, F. Barthelat, *J. Mech. Phys. Solids* **2014**, *68*, 66.

[4] A. Salamova, R. A. Hites. *Environ. Sci. Technol.* **2013**, 47, 349.

[5] a) W. C. Yan, P. Davoodi, S. Vijayavenkataraman, Y. Tian, W. C. Ng, J. Y. H. Fuh, K. S. Robinson, C. H. Wang, *Adv. Drug Delivery Rev.* **2018**, *132*, 270; b) R. F. Pereira, A. Sousa, C. C. Barrias, P. J. Bártolo, P. L. Granja, *Mater. Horiz.* **2018**, *5*, 1100.

[6] A. P. R. Johnston, C. Cortez, A. S.Angelatos, F. Caruso, *Curr. Opin. Colloid Interface Sci.* **2006**, *11*, 203.

[7] B. Wicklein, A. Kocjan, G. Salazar-Alvarez, F. Carosio, G. Camino, M. Antonietti, L. Bergström, *Nat. Nanotechnol.* **2015**, *10*, 277.

[8] a) P. Fratzl, R. Weinkamer, *Prog. Mater. Sci.* **2007**, *52*, 1263; b) U. G. K. Wegst, H. Bai, E. Saiz, A. P. Tomsia, R. O. Ritchie, *Nat. Mater.* **2015**, *14*, 23.

[9] D. Kokkinis, F. Bouville, A. R. Studart, *Adv. Mater.* **2018**, 30, 1705808.

[10] S. Rudykh, C. Ortizb, M. C. Boyce, *Soft Matter* **2015**, *11*, 2547.

[11] a) X. Y. Liu, H. W. Yuk, S. T. Lin, G. A.Parada, T. C. Tang, E. Tham, C. de la Fuente-Nunez, T. K. Lu, X. H. Zhao, *Adv. Mater.* **2018**, *30*, 1704821; b) N. D. Dolinski, Z. A. Page, E. B. Callaway, F. Eisenreich, R. V. Garcia, R. Chavez, D. P. Bothman, S. Hecht, F. W. Zok, C. J. Hawker, *Adv. Mater.* **2018**, *30*, 1800364; c) S. V Murphy, A. Atala, *Nat. Biotechnol.* **2014**, *32*, 773.

[12] a) B. M.Rauzan, A. Z. Nelson, S. E. Lehman, R. H. Ewoldt, R. G. Nuzzo, *Adv. Funct. Mater.* **2018**, *28*, 1707032; b) J. T. Muth, P. G. Dixon, L. Woish, L. J. Gibson, J. A. Lewis, *Proc. Natl. Acad. Sci. U. S. A.* **2017**, 114, 1832.

[13] a) G. Siqueira, D. Kokkinis, R. Libanori, M. K. Hausmann, A. S. Gladman, A. Neels, P. Tingaut, T. Zimmermann, J. A. Lewis, A. R. Studart, *Adv. Funct. Mater.* **2017**, *27*, 1604619; b) L. Y. Li, P. F. Zhang, Z. Y. Zhang, Q. M. Lin, Y. Y. Wu, A. Cheng, Y. X. Lin, C. M. Thompson, R. A. Smaldone, C. F. Ke, *Angew. Chem.* **2018**, *130*, 5199.

[14] a) K. Markstedt, A. Mantas, I. Tournier, H. M. Ávila, D. Hägg, P. Gatenholm, *Biomacromolecules* **2015**, *16*, 1489; b) H. Thakkar, S. Eastman, Q. Al-Naddaf, A. A. Rownaghi, F. Rezaei, *ACS Appl. Mater. Interfaces* **2017**, *9*, 35908.

[15] a) D. Kokkinis, M. Schaffner, A. R. Studart, *Nat. Commun.* **2015**, *6*, 8643.; b) C. Minas, D. Carnelli, E. Tervoort, A. R. Studart, *Adv. Mater.* **2016**, *28*, 9993.; c) L. Zorzetto, D. Ruffoni, *Adv. Funct. Mater.* **2019**, *29*, 1805888; d) C. Xu, B. Quinn, L. L. Lebel, D. Therriault, *ACS Appl. Mater. Interfaces* **2019**, *11*, 8499; e) J. Y. Liu, O. Erol, A. Pantula, W. Q. Liu, Z. R. Jiang,

K. Kobayashi, D. Chatterjee, N. Hibino, L. H. Romer, S. H. Kang, T. D. Nguyen, D. H. Gracias, *ACS Appl. Mater. Interfaces* **2019**, *11*, 8492.

[16] a) L. C. Hsiao, A. Z. M. Badruddoza, L. C. Cheng, P. S. Doyle, *Soft Matter* **2017**, *13*, 921; b) Y. C. Chao, S. Y. Mak, S. Rahman, S. P. Zhu, H. C. Shum, *Small* **2018**, *14*, 1802107.

[17] S. Q. Huan, R. Ajdary, L. Bai, V. Klar, O. J. Rojas, *Biomacromolecules* **2019**, 20, 635.

[18] a) N. A. Sears, P. S. Dhavalikar, E. M. Cosgriff-Hernandez, *Macromol. Rapid Commun.* **2016**, *37*, 1369; b) G. L. Ying, N. Jiang, S. Maharjan, Y. X. Yin, R. R. Chai, X. Cao, J. Z. Yang, A. K. Miri, S. Hassan, Y. S. Zhang, *Adv. Mater.* **2018**, *30*, 1805460.

[19] T. Yang, Y. Hu, C. Y. Wang, B. P. Binks, *ACS Appl. Mater. Interfaces* **2017**, *9*, 22950.

[20] M. R. Sommer, L. Alison, C. Minas, E. Tervoort, P. A. Ruhs, A. R. Studart, *Soft Matter*, **2017**, *13*, 1794.

[21] M. R. Sommer, M. Schaffner, D. Carnelli, A. R. Studart, *ACS Appl. Mater. Interfaces* **2016**, *8*, 34677.

[22] a) J. Wu, G. H. Ma, *Small* **2016**, *12*, 4633; b) L. Bai, S. Q. Huan, W. C. Xiang, O. J. Rojas, *Green Chem.* **2018**, *20*, 1571.

[23] L. Bai, S. Q. Huan, W. C. Xiang, L. Liu, Y. Yang, R. W. N. Nugroho, Y. M. Fan, O. J. Rojas, *ACS Sustainable Chem. Eng.* **2019**, *7*, 6497.

[24] B. D. Mattos, L. G. Greca, B. L. Tardy, W. L. E. Magalhães, O. J. Rojas, *Small* **2018**, *14*, 1801256.

[25] J. E. Smay, J. Cesarano, J. A. Lewis, *Langmuir* **2002**, *18*, 5429.

[26] A. Abbadessaa, M. Landínb, E. O. Blenkea, W. E. Henninka, T. Vermondena, *Eur. Polym. J.* **2017**, *92*, 13.

[27] a) P. Boltenhagen, Y. T. Hu, E. F. Matthys, D. J. Pine, *Phys. Rev. Lett.* **1997**, *79*, 2359; b) P.D. Olmsted, C. Y. D. Lu, *Phys. Rev. E* **1997**, *56*, R55.

[28] H. Tanaka, *Faraday Discuss.* **2012**, *158*, 371.

[29] a) D. Chandler, *Nature* **2005**, *437*, 640; b) H. Lee, C. H. Choi, A. Abbaspourrad, C. Wesner, M. Caggioni, T. T. Zhu, S. Nawar, D. A. Weitz, *Adv. Mater.* **2016**, *28*, 8425.

[30] J. Banhart, *JOM* **2000**, *52*, 22.

[31] P. A. Steward, J. Hearna, M. C. Wilkinson, *Adv. Colloid Interface Sci.* **2000**, *86*, 195.

[32] a) B. D. Mattos, O. J. Rojas, W. L. E. Magalhães, *J. Cleaner Prod.* **2017**, 142, 4206; b) X. Xu, B. Bai, H. Wang, Y. Suo, *ACS Appl. Mater. Interfaces* **2017**, 9, 6424.

Supporting Information

Two-Phase Emulgels for Direct Ink Writing of Skin-bearing Architectures

Siqi Huan, Bruno D. Mattos, Rubina Ajdary, Wenchao Xiang, Long Bai, Orlando J. Rojas**

Preparation of chitin nanofiber. Alpha-chitin was purified from fresh crabs that were acquired in the local market (Helsinki harbor, Finland). Briefly, crab shells were pretreated by alternating 1 M HCl and 1 M NaOH immersion for 24 h of each step, with at least 3 cycles. The obtained residual solid was decolorized by treating with 0.5 wt% $NaClO_2$ solution (pH 5.0, acetic acid) for 2 h at 70 °C. The purified flake-like residues were fully washed with distilled water before crushing into small pieces with a household blender. Before nanofibrillation of chitin, purified chitin was treated with 33 wt% NaOH solution at 90 °C for 3.5 h to achieve partially deacetylated chitin (DE-chitin). The DE-chitin was thoroughly washed with distilled water to reach neutral pH. The liquid-to-solid ratio used in deacetylation was 25 ml/g. The degree of deacetylation of DE-chitin was 27.3% *via* conductivity titration measurement.[1] DE-chitin was re-dispersed in water at a concentration of 0.2 wt%, followed by pH adjustment (3.0) with acetic acid under vigorous stirring. The obtained coarse suspension was homogenized to fine suspension by using a high-speed blender (T-25 Ultra-Turrax Digital Homogenizer, IKA, Germany) at room temperature. Subsequently, ultra-sonication was continuously applied to the fine suspension using a titanium tip sonicator (Sonifier 450, Branson Ultrasonics Co., Danbury, CT, USA) under a power level set at 50% with alternating on-off cycles (40 min, 5 s - 2 s, respectively). The obtained nanofibrillated chitin suspension was centrifuged at 10000 rpm for 5 min to remove large particles, and the supernatant was collected as a dispersion of chitin nanofiber (ChNF).

Characterization of fibrillar nanoparticles for Pickering emulsions. The morphology of CNF, ChNF and CNF/ChNF mixture was observed by transmission electron microscopy (TEM, JEM-2800, JEOL, Japan). A drop of diluted suspension (0.005%) was deposited on the electron microscope grid coated with carbon-reinforced formavar film, and negatively stained by uranyl acetate solution before room temperature drying. Observation was conducted at an acceleration voltage of 120 kV.

Zeta potential was measured using a Zetasizer Nano (ZS-90, Malvern Instruments, Worcestershire, UK). The samples were diluted with water at proper pH prior to measurement in order to avoid multiple scattering effects. All measurements were carried out on freshly prepared duplicate samples, and three runs were performed for each sample.

The transmittance of the suspensions (300 to 800 nm wavelength) was measured using a UV-2550 UV-vis spectrophotometer (SHIMADZU, Kyoto, Japan) operated at room temperature. The samples were placed within 1 cm path length optical cells. All measurements were carried out on freshly prepared duplicate samples.

Morphology of Pickering emulsions. The emulsion droplets were examined by confocal with a 40× oil immersion objective lens (Leica DMRXE, Leica, Germany). 100 μL of the sample was dyed with 10 μL of Nile red solution (1 mg/mL ethanol). After homogeneously mixing with a pipette, 6 μL of the dyed sample was placed on a microscope slide and covered with a glass coverslip (Assistent, Sondheim, Germany). The coverslip was quickly fixed with a nail polish to avoid evaporation.

The simultaneous observation of CNF/ChNF and oil phase in Pickering emulsions were imaged by Zeiss Axio Observer optical microscope (Zeiss, Germany) with a 63× oil immersion lens. The oil was dyed by Nile red prior to emulsion preparation. The CNF/ChNF was stained by Calcofluor white prior to observation. Sample preparation procedure was similar as confocal. The excitation and emission spectrum for Calcofluor white were 365 nm and 435 nm, respectively. The merging of obtained fluorescent images into a single image was processed

with ImageJ (imagej.nih.gov). The droplet size for emulsion obtained was an average value that counted at least 100 droplets.

Droplets's surface coverage. According to previous work,[1] the apparent total % coverage (*C*) of CNF/ChNF at the surface of PLA droplets was determined from the following relationship:

$$C = \frac{m_p D}{6h\rho V_{oil}}$$

where m_p is the mass of CNF/ChNF (0.5 wt%), *D* is mean droplet diameter (7.8 μm), *h* is the thickness of CNF/ChNF, ρ is the density of CNF/ChNF (1.51 g/cm^3), and V_{oil} is the volume of PLA/$CHCl_3$ used in the emulsion. The value of *h* for CNF/ChNF was assumed to be 14 nm. The water-to-oil ratio by volume was 1:1. Based on these parameters, *C* was calculated to be ~31%, which indicates a high likelihood that no free CNF/ChNF was dispersed in the aqueous phase after emulsion preparation: any ecess particles would be adsorbed onto the surface of the droplets to increase the surface coverage, thereby reducing the interfacial energy generated during emulsification.

Properties of the solid particles. Silica gel particles (40-75 μm, 0.7-0.9 cm^3/g pore volume) are porous, granular, lightweight form of silicon dioxide typically produced from sodium silicate. Fumed silica (0.2-0.3 μm) is a powder composed of submicron-sized amorphous silica spheres, which are burned in a flame of hydrogen and oxygen from silicon tetrachloride or quartz. Hydrophilic bentonite nanoclay ($Al_2O_3{\cdot}2SiO_2{\cdot}H_2O$, ≤ 25 μm) is an untreated hydrophobic clay material composed of hydrated aluminum oxide and silicon oxide. Iron (II, III) oxide (Fe_3O_4, <5 μm) is highly insoluble in aqueous solutions, containing at least one oxygen anion and one metallic cation. Hydroxyapatite powder ($[Ca_5(OH)(PO_4)_3]_x$, 2.5 μm, ≥100 m^2/g) is consisted of spherical or faceted high surface area oxide magnetic nanostructured particles.

The zeta potential of the particles was measured in suspensions prepared with Milli-Q water, pH 3.5. The pH was selected according to the value of CNF/PAA mixture, which can result in a similar aqueous environment for solid particles as in the hydrogels. The concentration in the suspension for each particle type was 0.05 wt%. Prior to the measurements, freshly prepared suspensions were vortexed for at least 20 s and immediately transferred to the measuring cuvette to perform the measurements. The refractive index and zeta potential for the different particles are listed in **Table S1**. The zeta potential for silica, fumed silica, nanoclay and hydroxyapatite was slightly negative at pH 3.5. On the other hand, the iron (II, III) oxide was positively charged (~ +24 mV) at pH 3.5, in agreement to data from the literature and indicating that that iron particles change to slight positive charge at acidic condition.[2]

Morphology of the emulgels. The morphology of emulgel/hydrogel precursor and post-crosslinked emulgel were visualized by optical microscopy (Leica DM 750, Leica, Germany) with 40× objective lens. A small amount of sample was placed onto a microscope slide and covered with a glass coverslip. The precursor was observed after 30 min preparation, and the crosslinked emulgel was placed at room temperature at least 2 h after crosslinking before observation.

Effect of emulsion droplet size and PLA concentration on the skin formation. The effect of the emulsion droplet size and PLA loading level on the formation of skin structures was investigated. A sonication time of 30 s was applied to generate Pickering emulsions with different droplet sizes. To obtain emulsion samples with different PLA loadings (2 and 8 wt%), PLA/$CHCl_3$ solution containing different PLA concentrations were used as oil phase in the emulsification. For both samples, the rest of the procedure to prepare printable inks was kept the same as indicated in the main text.

The droplet size at shorter sonication duration was approximately 15 μm (**Figure S7a**), which was larger than the one discussed in the main text. After preparing the emulgel ink and 3D printing following the same protocol as indicated in the main text, cubic grids were

successfully obtained. The corresponding SEM images presented a clear skin-bearing structure (**Figure S7b**). The results demonstrate that the emulsion droplet size has no significant effect of on the stratification of emulgel upon printing.

The emulsion droplet size of 8 wt% PLA was slightly larger than that of 4 wt% PLA owing to the higher viscosity of the organic phase upon emulsification (**Figure S8a**). Emulgel inks with high PLA content were subjected to oscillatory rheological measurements, which showed a similar yield stress behavior compared to that for 4 wt% PLA loading (**Figure S8c**), indicating a similar printing behavior for the 8 wt% PLA sample in comparison with that of the 4 wt% PLA emulgel. A skin structure for 8 wt% PLA sample was clearly observed in SEM images (**Figure S8d**). However, the coverage was not as extensive as that observed for the 4 wt% PLA sample, which is likely a result of the higher shear viscosity of the 8 wt% PLA emulsion (**Figure S8b**), leading to a less efficient phase separation. We note that the emulgel containing 2 wt% PLA in the emulsion phase also showed a skin structure but with large cracks and broken areas (**Figure S8e**). Hence, a low PLA loading in the emulsion phase impairs skin formation during printing. In summary, the effect of PLA concentrations in the Pickering emulsions indicated that skin structures were formed at all the concentrations tested but differences in coverage and quality were noted. A \n optimal concentration of 4 wt% PLA was chosen in this work.

Wettability of polypropylene and stainless-steel substrates. The wettability of printing needles (polypropylene or stainless steel) was evaluated by measuring the contact angle (CA) of PLA/$CHCl_3$-in-water Pickering emulsions onto both of the substrates. CA on the substrates were measured using a CAM 200 optical contact angle meter (KSV Instruments Ltd.). Sessile emulsion droplets (10 μL) were placed on the substrate by an auto-pipette and allowed to spread freely on the surface. Droplet imaging was recorded by a high-resolution CCD camera at 1 s intervals for 10 s. The CA was determined using the KSV CAM 200 software by analyzing droplet imaging. All the experiments were carried out on freshly prepared, duplicate samples.

The droplet image and corresponding CA values for both polypropylene and stainless-steel substrates are shown in **Figure S9**.

Mechanical strength of the grids. Compression tests of printed grids after freeze-drying were conducted by using a dynamic mechanical analysis (DMA, TA Instruments Q800, United States) equipped with a 18N load cell. The measurements were performed in displacement control mode at a rate of 0.05 N/min until reaching the final loading level of 18N, see **Figure S12**. Three replicates were performed for each formulation.

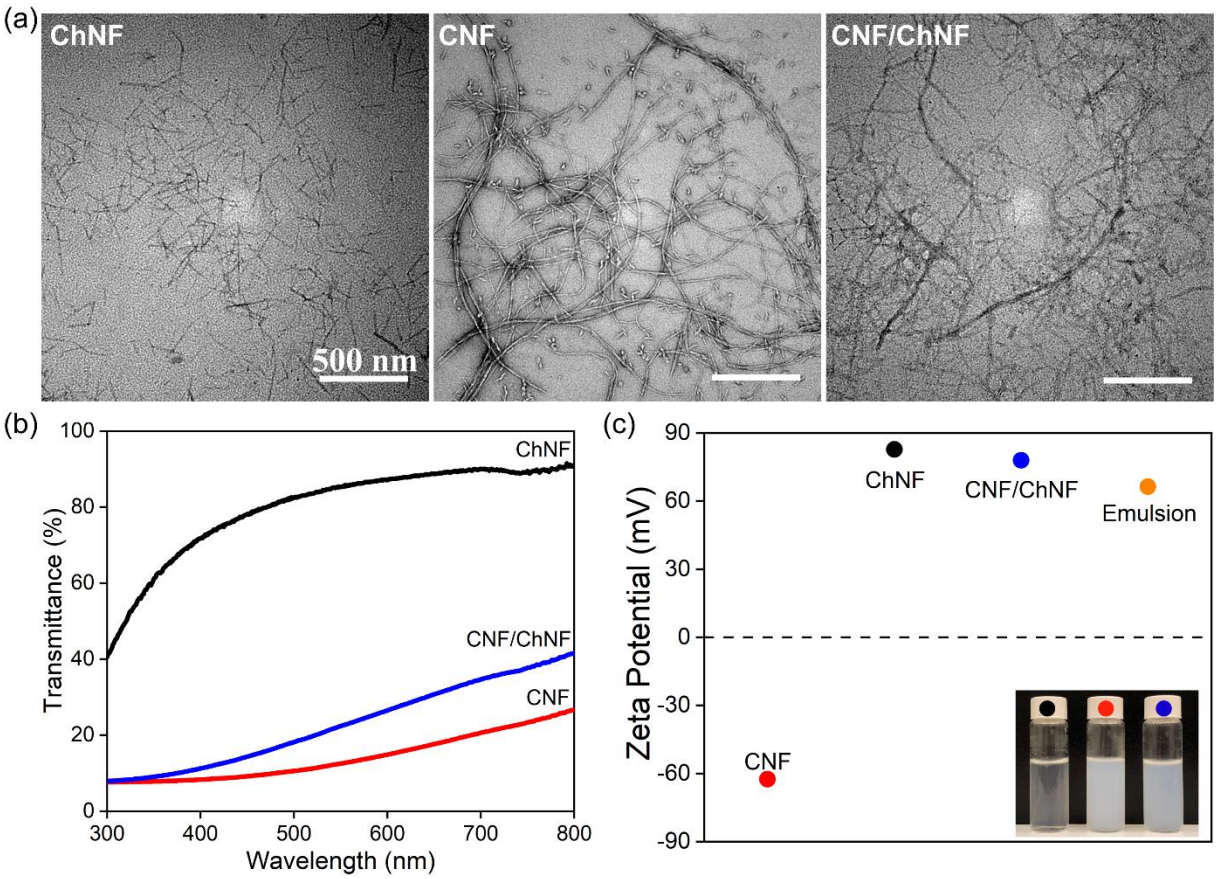

Figure S1. (a) Transmission electron microscopy (TEM) images of chitin nanofiber (ChNF), cellulose nanofibrils (CNF), and the mixture of CNF/ChNF. The scale bar is 500 nm. (b) Transmittance of ChNF, CNF and CNF/ChNF suspensions. The concentration for all the measurement was 0.3 wt%. (c) Zeta potential of the suspensions and Pickering emulsion. The insert in (c) is the visual appearance of the suspensions (0.3 wt%). All the measurements were performed at ambient temperature.

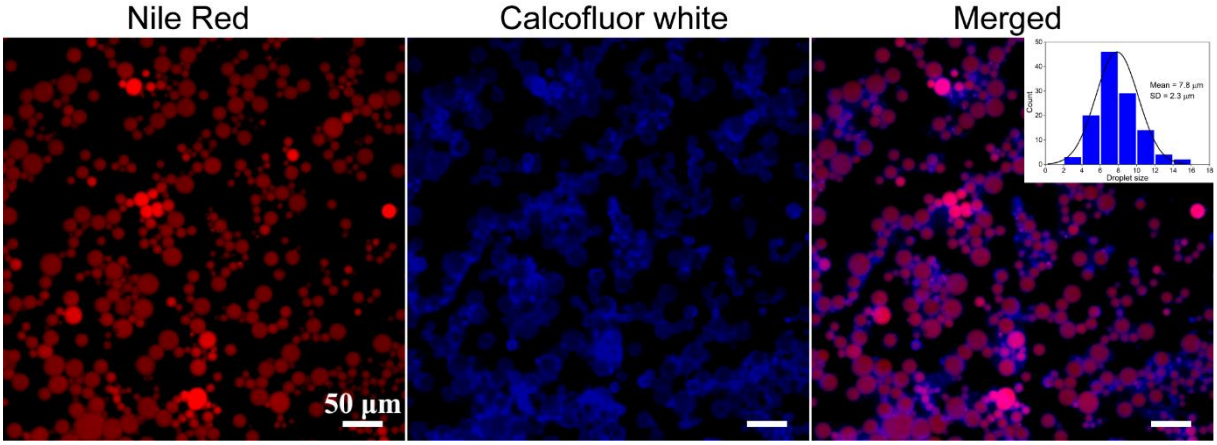

Figure S2. Fluorescent microscopy images of CNF/ChNF-stabilized PLA/$CHCl_3$-in-water Pickering emulsions. Prior to observation, the oil phase was dyed by Nile Red (left), and the mixture of CNF/ChNF was stained by Calcofluor white (middle). The insert in merged image (right) is the histogram of droplet diameter. The scale bar is 50 µm.

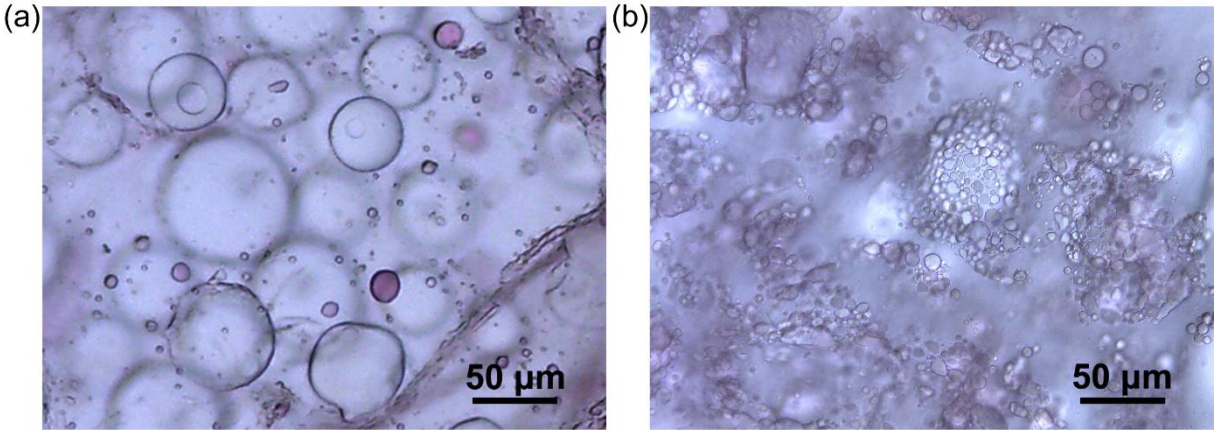

Figure S3. Optical microscope images of two-phase emulgels (a) before and (b) after alkali-induced crosslinking. Sample ESR4 was used for imaging. The scale bar is 50 µm.

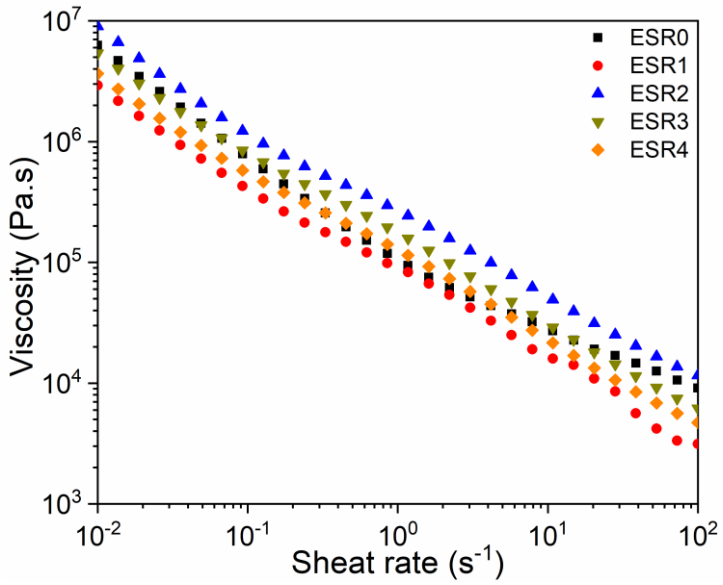

Figure S4. Flow curves of the apparent shear viscosity as a function of shear rate for all-in-one two-phase emulgel inks at different emulsion loadings (ESR0 to ESR4). All the measurements were performed at room temperature.

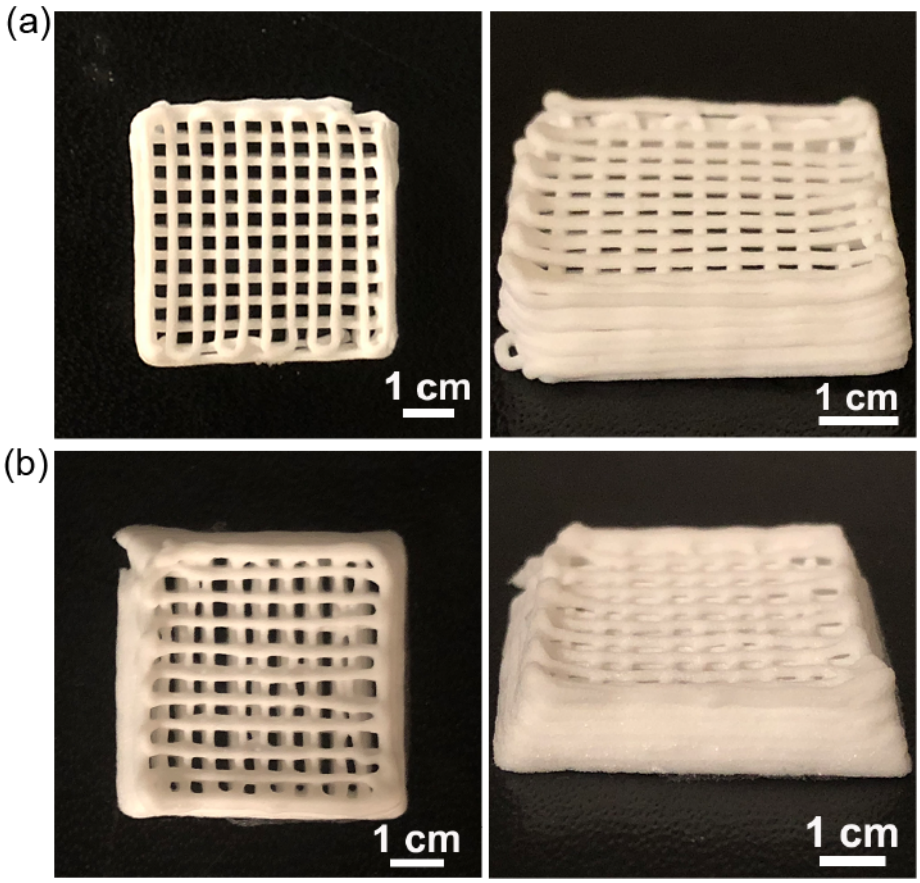

Figure S5. Top (left) and side (right) view of the printed cubic grids of (a) ESR0 (no emulsion) and (b) ESR3. The printed grids were freeze-dried at least 2 days before characterization. The scale bar is 1 cm for (a) and (b).

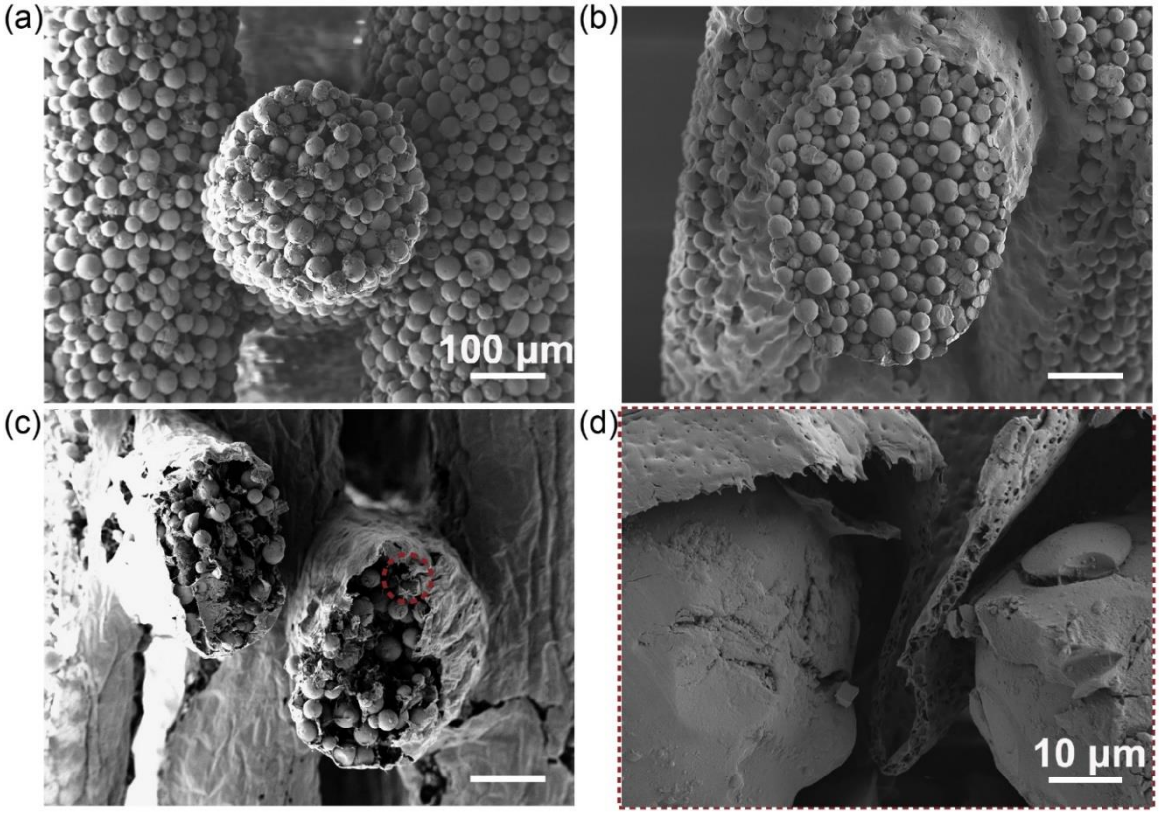

Figure S6. Scanning electron microscopy (SEM) images of the cross-section of the printed cubic grids of (a) ESR0, (b) ESR2, and (c) ESR4. (d) Cross-section of ESR4 at higher magnification. The scale bar is 100 µm for (a) to (c), and 10 µm for (d).

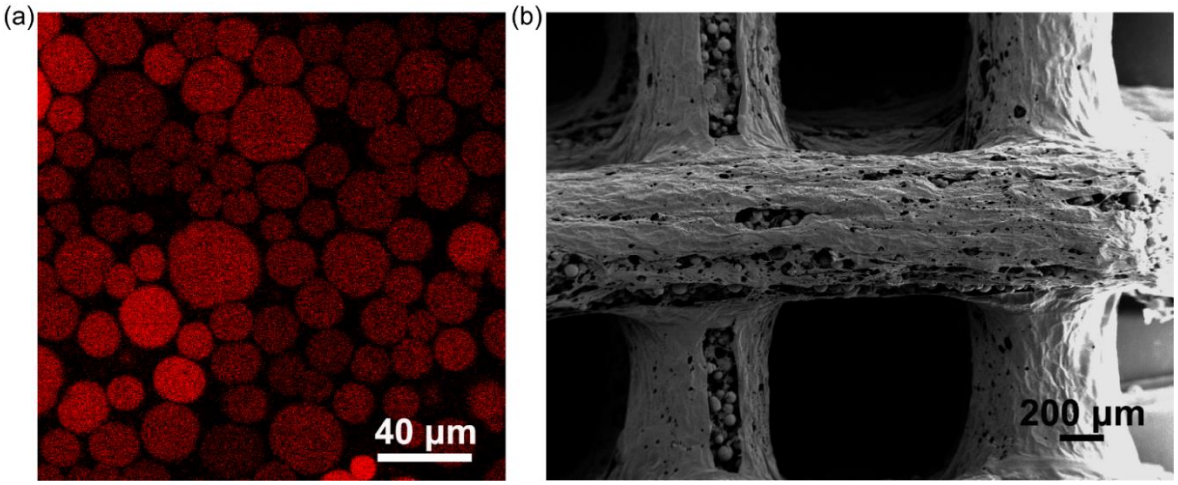

Figure S7. (a) Confocal image of PLA/$CHCl_3$-in-water Pickering emulsion stabilized by CNF/ChNF mixture. The sonication duration was 30 s to produce droplets with large size, and other procedure was the same as that of 60 s-sonication. (b) SEM image of the printed structure prepared from emulgel of ESR4. The emulsion phase used in such ink was from (a). The needle size was 0.63 mm. The grid was freeze-dried at least 2 days before imaging. The scale bar is 200 µm.

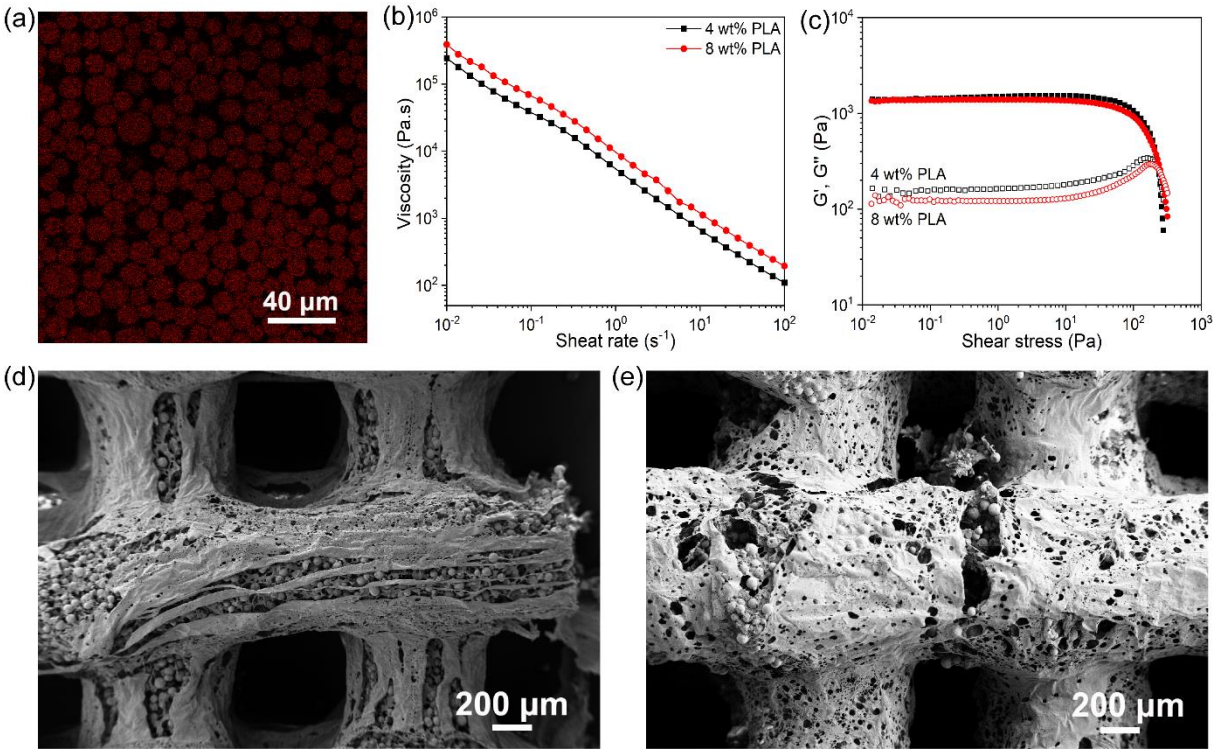

Figure S8. (a) Confocal image of PLA/$CHCl_3$-in-water Pickering emulsion stabilized by CNF/ChNF mixture at 8 wt% PLA concentration dissolved in chloroform. (b) Shear thinning and (c) oscillatory rheology of the emulgels with 8 wt% PLA. (d) SEM image of the printed structure prepared from emulgel of ESR4 with (d) 8 and (e) 2 wt% PLA, respectively. The needle size was 0.63 mm. The grids were freeze-dried at least 2 days before imaging. The scale bar is 200 µm.

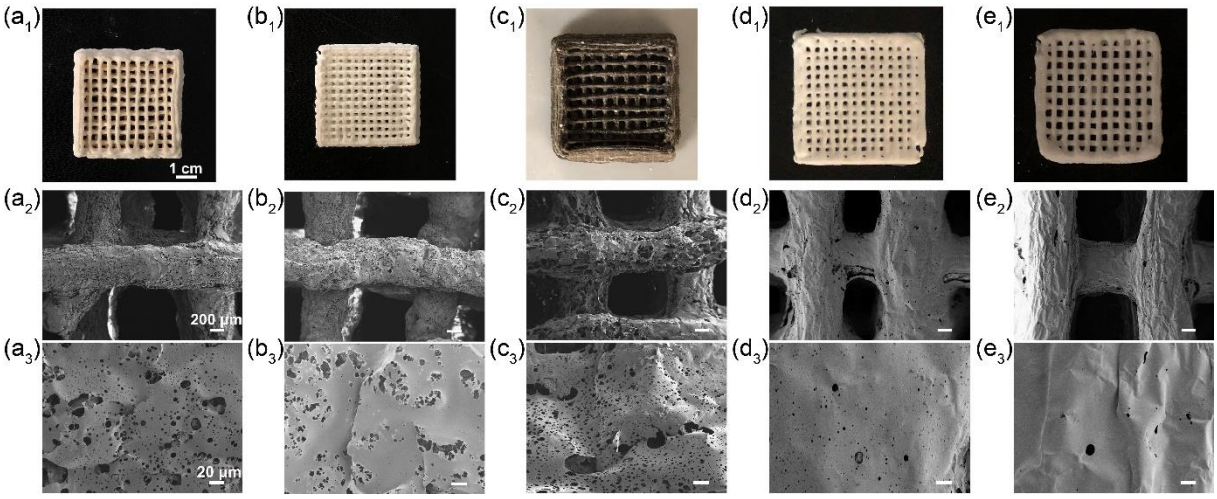

Figure S9. Universal test for the formation of visual appearance and skin formation from all-in-one two-phase emulgel inks with supporting materials of (a_1, a_2, a_3) nanoclay, (b_1, b_2, b_3) fumed silica, (c_1, c_2, c_3) iron, and (d_1, d_2, d_3) hydroxyapatite, and with (e_1, e_2, e_3) polystyrene as the polymer phase in emulsion. The emulsion to supporting material ratio was 45:6 for all the samples. All the printed grids were freeze-dried at least 2 days before imaging. The scale bar is 200 µm for (a_1) to (e_1), and 20 µm for (a_2) to (e_2).

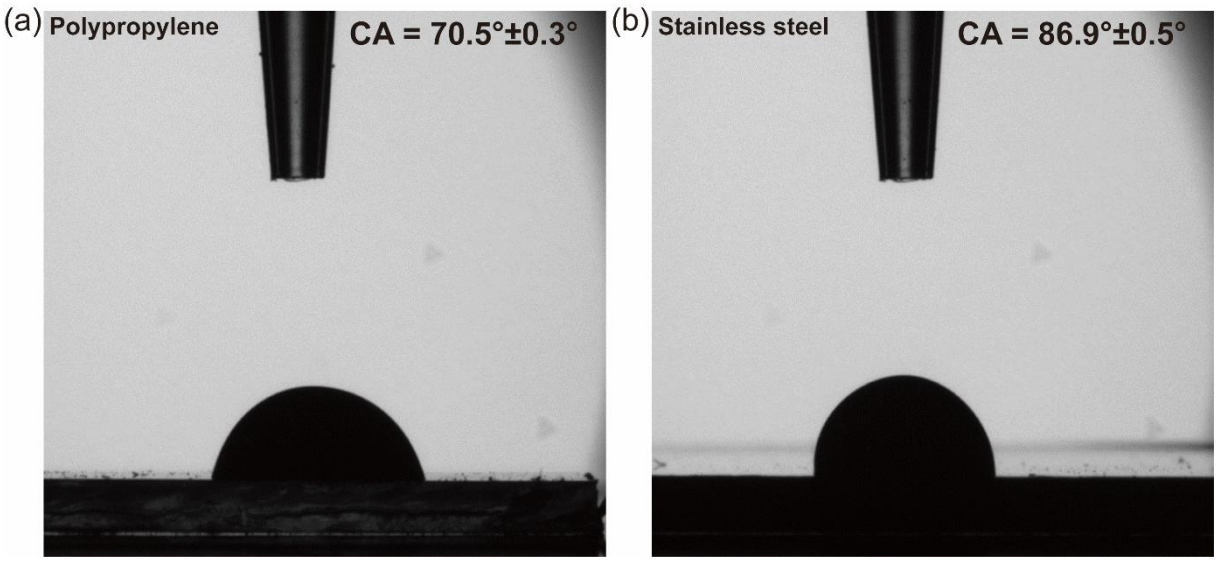

Figure S10. Contact angle (CA) of PLA/$CHCl_3$-in-water Pickering emulsions on (a) polypropylene and (b) stainless steel. The CA value for each substrate is indicated in (a) and (b). All measurements were carried out at ambient temperature.

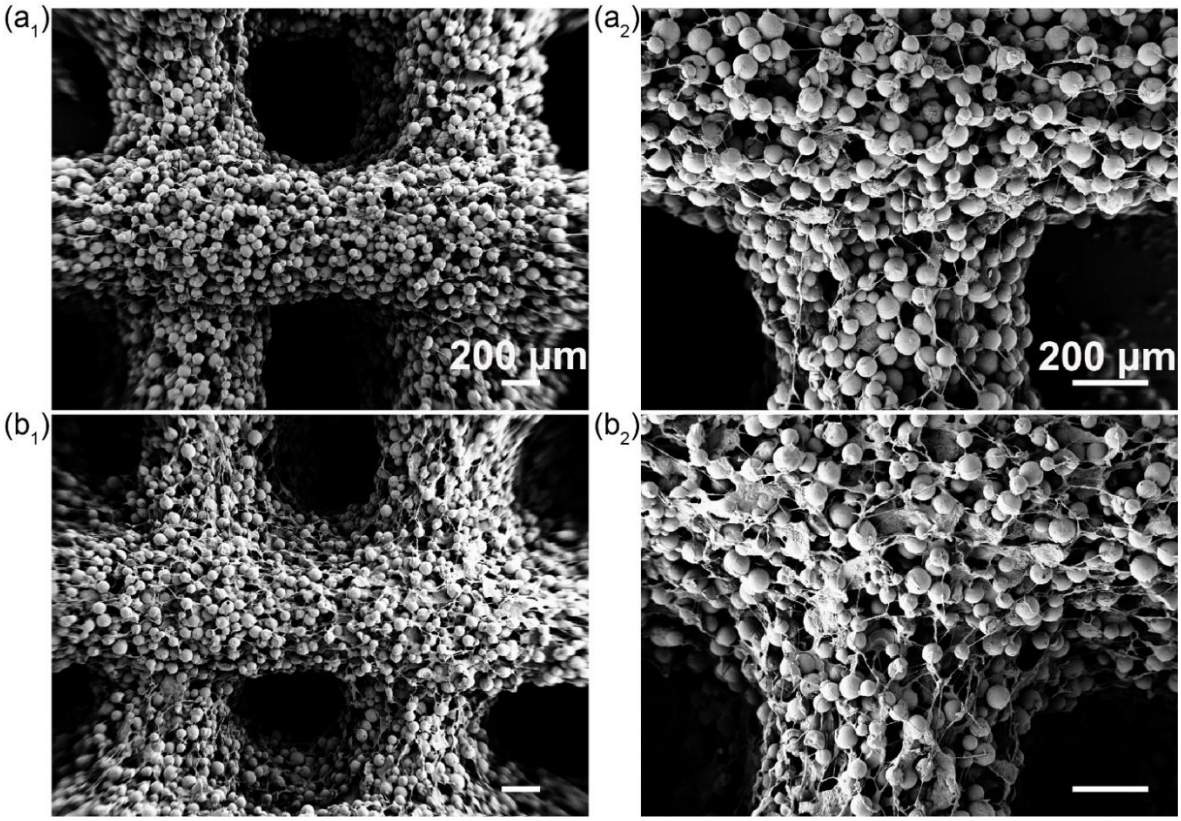

Figure S11. SEM images of the printed cubic grids prepared from inks without loading Pickering emulsions. The silica concentration for (a_1, a_2) and (b_1, b_2) is ESR01 (12 wt%) and ESR02 (6 wt%), respectively. The scale bar is 200 μm for (a_1) and (b_1), and 200 μm with higher magnification for (a_2) and (b_2).

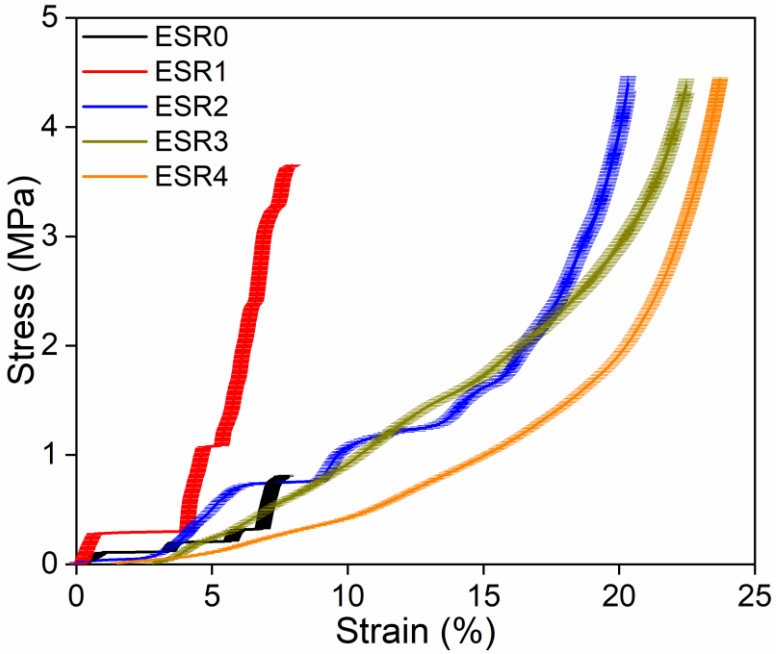

Figure S12. Compression profiles for printed cubic grids obtained from emulgels ESR0 to ESR4. All printed grids were freeze-dried at least 2 days before testing. All measurements were conducted at ambient temperature.

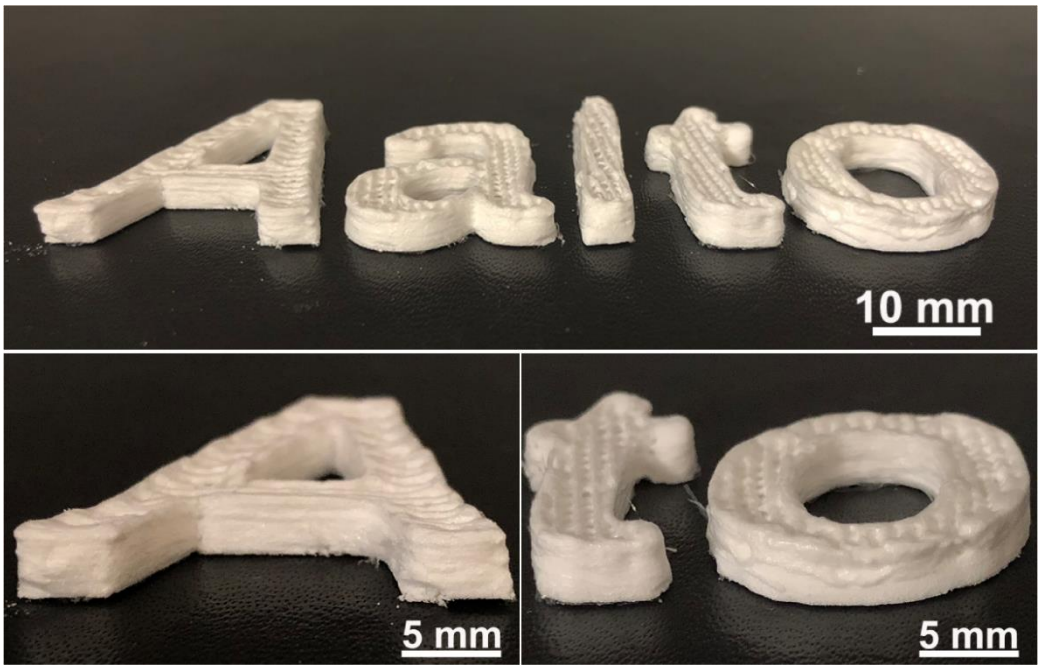

Figure S13. Side view of the printed "letters-Aalto" from emulgel ink ESR4. The scale bar is 10 mm for top image, and 5 mm for bottom images.

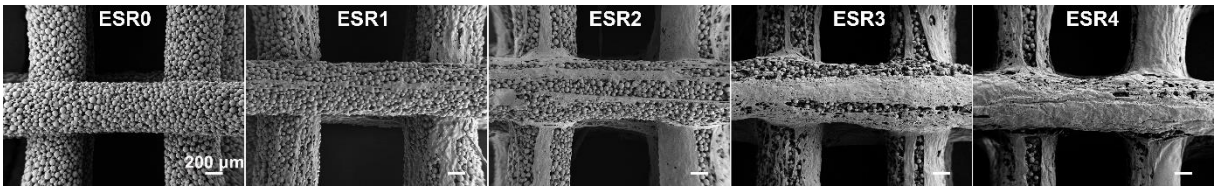

Figure S14. SEM images of the printed cubic grids with different emulsion loadings (ESR0 to ESR4) after encapsulating model cargo (sodium salicylate) into silica particles prior to writable ink preparation. All the printed grids were freeze-dried at least 2 days before imaging. The scale bar is 200 µm.

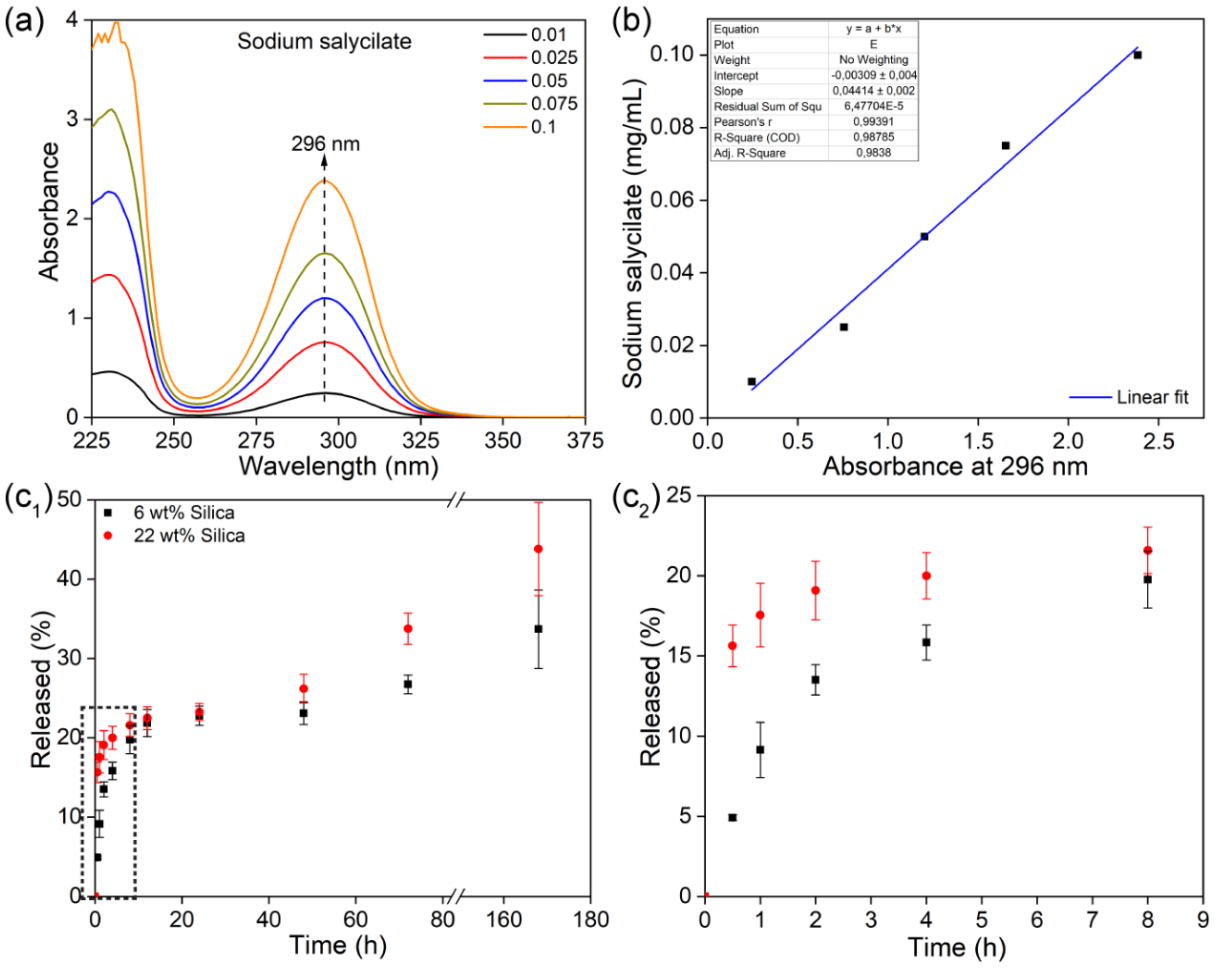

Figure S15. UV spectra of sodium salicylate solutions at given concentration (a) acquired to prepare the calibration curve for the drug release and quantification in water (b). Release profiles for grids containing different loadings of the solid silica fillers in the hydrogel (c_1 and c_2). c_2 details the first 8 h of release.

Table S1. Refractive index (RI) and zeta potential of different solid particles

	RI	Zeta potential (mV)
CNF/PAA	1.544	-33.7 ± 3.9
Silica particle	1.475	-22.8 ± 0.7
Fumed silica particle	1.470	-16.1 ± 0.9
nanoclay	1.540	-32.9 ± 0.3
Iron (II, III) oxide	2.918	24.8 ± 0.5
Hydroxyapatite	1.635	-14.4 ± 0.6

Table S2. Coefficient of determination and release rate coefficients of the kinetic models applied as a tentative to explain the release of drug out from the printed skin-bearing grids

Model		ESR0	ESR1	ESR2	ESR3	ESR4
Zero	r^2	0.83	0.73	0.86	0.60	0.86
$Q_t = k_0 * t$	k_0	0.017 ± 0.004	0.008 ± 0.003	0.007 ± 0.002	0.006 ± 0.003	0.006 ± 0.001
Elovich	r^2	0.99	0.94	0.97	0.89	0.96
$Q_t = k_E * \ln t$	k_E	0.052 ± 0.003	0.025 ± 0.003	0.021 ± 0.002	0.020 ± 0.004	0.017 ± 0.002
Higuchi	r^2	0.93	0.85	0.94	0.82	0.94
$Q_t = k_H * t^{0.5}$	k_H	0.065 ± 0.010	0.031 ± 0.007	0.027 ± 0.004	0.024 ± 0.008	0.021 ± 0.003
Korsmeyer-Peppas	r^2	3	0.92	0.96	0.84	0.95
$Q_t = k_{KP} * t^n$	k_{KP}	0.0815	0.1398	0.1077	0,1025	0.0606
	n	1.106 ± 0.176	0.3867 ± 0.065	0.414 ± 0.045	0.423 ± 0.107	0.536 ± 0.069
Peppas-Sahlin	r^2	0.97	0.91	0.94	0.94	0.94
$Q_t = k_1 * t^{0.5} + k_2 * t$	k_1	0.158 ± 0.037	0.096 ± 0.030	0.058 ± 0.020	0.073 ± 0.010	0.043 ± 0.015
	k_2	-0.025 ± 0.009	-0.018 ± 0.008	-0.007 ± 0.005	-0.014 ± 0.004	-0.006 ± 0.004

Note: r^2 = coefficient of determinaiton; t = time; Q_t = fraction of drug released at the time t; n= release exponent of the Korsmeyer-Peppas kinetic model; k_0, k_E, k_H, k_{KP}, k_1 and k_2 = release rate coefficients of each respective kinetic model.

References

[1] L. Bai, S. Q. Huan, W. C. Xiang, L. Liu, Y. Yang, R. W. N. Nugroho, Y. M. Fan, O. J. Rojas, *ACS Sustainable Chem. Eng.* **2019**, 7, 6497.

[2] L. Bai, W. C. Xiang, S. Q. Huan, O. J. Rojas, *Biomacromolecules* **2018**, 19, 1674.

[3] X. P. Meng, J. Ryu, B. Kim, S. H. Ko, *Clin. Nutr. Res.* **2016**, 5, 172.